

**The present work was submitted to the Faculty of Engineering**

**Assessment of soil erosion and geomorphological mapping in and around Baganuur  
using satellite-based data**

## **Bachelor Thesis**

by

**Bilguundalai Batkhuyag**

Supervisor 1 / Examiner 1

**Dr. Martin Knippertz**

Supervisor 2 / Examiner 2

**M.Sc. Enkhjargal Sodnomdarjaa**

Ulaanbaatar/Nalaikh, 2022

## Statutory Declaration

Batkhuyag, Bilguundalai

15348204550086

\_\_\_\_\_  
Last Name, First Name

\_\_\_\_\_  
Student ID Number

I hereby affirm in lieu of an oath that I provided the submitted bachelor thesis

I did not use any sources other than those stated. In case that the work is additionally submitted on a data medium, I declare that the written and the electronic form are completely identical. The work was not submitted in the same or similar form to any examination authority.

Ulaanbaatar, 05/16/2022

\_\_\_\_\_  
Place, Date

\_\_\_\_\_  
Signature

## **Abstract**

Satellite photography and remote sensing in general are becoming more important not only in the environmental sciences, but also in other fields such as economics, engineering, politics, archeology, and so on. As a result, this thesis will use satellite imagery and remote sensing to investigate erosion and geomorphology in the remote area of Baganuur, which houses one of Mongolia's largest open cast coal mines. The mine supplies a significant amount of coal to Ulaanbaatar's main thermal power plants, and while past examinations have revealed a link between the mine and pollution, most of the studies were conducted within the mine and not outside of it. In

The RUSLE equation used to calculate soil erosion in the Baganuur area in July and October of 2018 showed that the Baganuur region was under low risk of erosion hazard from rainfall and runoff. In addition, the method was also able to identify the difference of erosional rate between different seasons. The second goal of creating a geomorphological map was completed using a morphometric technique. There are 10 different landform classes and five different sub-basins in the Baganuur area.

Furthermore, the CORONA satellite picture, which had been georeferenced to aid in the geomorphological study, was discovered to be ineffective and could only be used in a limited way at this time.

## Contents

Abstract.....	iii
1 Introduction .....	2
2 State of the Art .....	3
2.1 Geomorphology .....	3
2.2 Soil Erosion .....	8
2.2.1 Effects of vegetation and rainfall .....	9
2.2.2 Effect of wind .....	10
2.2.3 Anthropomorphic influence .....	12
2.3 Revised Universal Soil Loss Equation (RUSLE).....	16
2.4 Corona Satelite images.....	17
2.5 Area of Study .....	19
2.5.1 Soil & Vegetation .....	20
2.5.2 Climate .....	21
3 Methodology .....	22
3.1 Georeferencing Corona Satelite imagery .....	22
3.1.1 Georeferencing process.....	22
3.1.2 Transformations.....	25
3.1.3 Technical limitations of CORONA images.....	26
3.2 RUSLE Calculations .....	29
3.2.1 Rainfall erosivity (R factor).....	29
3.2.2 Soil erodibility (K factor) .....	31
3.2.3 Topographic steepness factor (LS factor) .....	34
3.2.4 Land cover and management factor (C factor).....	35
3.2.5 Conservation practice (P factor).....	37
3.3 Morphometry analysis.....	38

3.3.1	TPI analysis .....	38
3.3.2	Watershed analysis .....	40
4	Results & Discussion.....	41
4.1	TPI based slope & landform classification.....	41
4.2	DEM based watershed analysis .....	44
4.3	Erosion .....	45
5	Conclusion .....	49
6	References.....	50
7	Appendices .....	52

## List of figures

Figure 1.	TPI values in relation to slope position (source: Weiss 2001 [9]).....	5
Figure 2.	TPI value in relation to its annulus area (source: Weiss 2001 [9]) .....	5
Figure 3.	River basins of Mongolia .....	7
Figure 4.	Flow direction, Flow accumulation and watershed components in ArcGIS (source: [12, 13]).	8
Figure 5.	Global soil erosion rate of 2012 (Source: An assessment of the global impact of 21'st century land use and change on soil erosion [35]).....	9
Figure 6.	Relationship between Effective precipitation and Sediment yield in USA (source: Dynamics Interactions of Life and its Landscapes [18]) .....	10
Figure 7.	Relationship between critical sheer velocity and grain size. (source: Soil erosion and conservation [14]) .....	11
Figure 8.	Wind erosion hazard map of Mongolia. (source: Wind erosion hazard assessment of the Mongolian Plateau using FCM and GIS techniques [36]) .....	12
Figure 9.	Typical impact points of the physical and geographical system and anthropogenic activities (source: anthropomorphic Geology [20]) .....	13
Figure 10.	Dirt piles used to prevent sediment washing from the Baganuur mines waste tips. ....	15
Figure 11.	CORONA satellite imagery example .....	17

Figure 12. Area of study.....	19
Figure 13. Baganuur area soil and vegetation typing (source: [41]).....	21
Figure 14. Georeferencing menu .....	22
Figure 15. Georeferencing: Fit to Display command .....	22
Figure 16. Georeferencing intended location.....	23
Figure 17, Georeferencing menu: Add Control Points, Select Link, Zoom to Selected Link, Delete Link, View Link Table .....	23
Figure 18. A: Source control points, B: Ground Control Points.....	24
Figure 19. Mosaicked CORONA satellite imagery.....	25
Figure 20. ArcMap's Polynomial transformations (source: []).....	26
Figure 21. Example of 1'st, 2'nd and 3'rd order transformations on a georeferenced image with unevenly distributed control points .....	26
Figure 22. Distortion of CORONA satellite imagery.....	27
Figure 23. Shadow developed by the CORONA image.....	28
Figure 24. Data sources for each RUSLE factor .....	29
Figure 25. Raster to points transformation example .....	30
Figure 26. A: Average annual precipitation of Baganuur in [ $\text{mm}\cdot\text{year}^{-1}$ ], B: R factor of Baganuur in [ $\text{MJ}\cdot\text{mm}\cdot\text{h}^{-1}\cdot\text{ha}^{-1}\cdot\text{year}^{-1}$ ].....	31
Figure 27. K factor of Baganuur area, determined via field survey and soil texture identification.....	32
Figure 28. Kusle factor calculated from global soil classification map.....	34
Figure 29. Baganuur LS factor source: Enkhjargal (2022).....	35
Figure 30. NDVI value of Baganuur in October and July .....	36
Figure 31. C factor value of Baganuur in October and July .....	37
Figure 32. TPI 200 and TPI 1000 .....	40
Figure 33. Outflow point example of watershed 2.....	40
Figure 34. Landform classification derived from TPI200 (A) and TPI1000 (B) .....	42
Figure 35. Landform classification based on combination of TPI200 and TPI1000.....	43

Figure 36. DEM- derived topographic attributes of Baganuur (A-D) .....	43
Figure 37. Baganuur flow direction - A, Baganuur flow accumulation - B .....	44
Figure 38. Baganuur watershed mapping .....	45
Figure 39. Soil loss of 2018/10 overlaid with landform mapping .....	46
Figure 40. Annex 1 zoomed to a scale of 1:25"000 - A: Baganuur settlement area, B: Dirt roads, C: Mountain ridges, D: North side of the Baganuur open cast mine.....	48

**List of tables**

Table 1. Different factors of geomorphology.....	3
Table 2. RUSLE factors .....	16
Table 3. K <sub>USLE</sub> factor parameters.....	33
Table 4. Topsoil propertie sof Luvic Castanozems and Lithosols derived from the FAO global soil classification .....	33
Table 5. Slope class thresholds for TPI.....	38
Table 6. Landform class threshold for TPI's .....	39
Table 7. Cell count and % coverage of each landform class of landform classification of TPI200 and TPI1000.....	42
Table 8. Cell count and % coverage of each landform class of landform classification based on TPI200xTPI1000.....	43
Table 9. Erosion risk class ratio and their corresponding areas in % for 2018.....	47

**List of graphs**

Graph 1. Stacked percentages of the slope position classes from different neighborhood classes (source: GIS-based landform and LULC classifications in the Sub-Himalayan Kaljani Basin [40]) .....	6
Graph 2. Total livestock count of Mongolia between 1960 and 2021 with a five-year interval (source: [39]) .....	14
Graph 3. Baganuur district temperature and precipitation graph (source: [38]).....	21

## **Acknowledgements**

First of all, I would like to thank my first supervisor Professor Martin Knippertz for supporting and giving me advice during my thesis and guiding me. I would also like to thank my second supervisor Enkhjargal Sodnomdarjaa for not only teaching me the necessary methods and techniques for working on satellite imagery and remote sensing but also providing me with essential data that were crucial to this thesis. Without the help of these supervisors, my work would not have been possible.

I would also like to give an additional thank you to Lukas Dörwald of Aachen University for giving me suggestions and advice on CORONA imagery.

# 1 Introduction

This Bachelor Thesis which was proposed by Prof. Martin Knippertz from Aachen university, focusses on geomorphological/ erosional forms in and around Baganuur (Mongolia) using satellite imagery. will also include a detailed guide on how to geo-reference CORONA satellite images with the purpose of creating a manual of the process for the Mongolian Science community and creating a digital map of the Baganuur area before it was influenced by anthropomorphic activities [e.g., mining activities].

To give a brief overview of Baganuur, it is one of Ulaanbaatar's remote districts, located around 130 kilometers east of the capital city and covering over 620 square kilometers [1]. The area contains the main Baganuur settlement, ger areas, small patches of croplands, Kherlen river and most importantly the Baganuur open cast coal mine which provides brown coal to a majority of the main Ulaanbaatar powerplants and several smaller thermal powerplants located throughout Mongolia. The mine itself was originally developed in 1978 where it continuous to supply coal with an estimated capacity of 4 million tons per year [2]. While there has been no direct correlation between mining and soil erosion in Baganuur, a previous study indicates that the Baganuur coal mine has adverse impact on the surrounding water quality which includes carbon weathering, cation exchange processes, softening, dissolution of evaporate minerals and the possible generation of  $\text{SO}_4$  and  $\text{NO}_3$  [3]. In addition, the mines overburdens and waste tips become a major source for air pollution and wind erosion which creates a hazardous environment for the mine's workers and the local population of Baganuur [3].

However, since the main topic of this thesis is soil erosion, other forms of erosion and environmental pollution will be briefly explored in the State of Art section of this paper, while a majority of the paper will cover RUSLE equations, CORONA images and geomorphometric analysis.

## 2 State of the Art

Geomorphology is the study of the formation and evolution of topographic features at or near the Earth's surface caused by exogenic or endogenic factors. Erosion is the major focus of this study and one of the most important geomorphological processes. As a result, the first half of the section will go through the fundamental concepts of geomorphology, how it is categorized, and the many research methodologies for investigating geomorphology. Following that, it will discuss the many forms of erosion, the factors that influence them, and the current condition of erosion on a global and Mongolian scale. The latter half will explore the origins of RUSLE equation and how it is used for calculating soil loss. Finally, this section will include general information on the history of CORONA photos, their initial purpose, and how they might be used in today's day and age.

### 2.1 Geomorphology

The study of the qualities of the earth's surface and the changes that occur on it is known as geomorphology. As such, it is a discipline that examines the current state of landforms, land-surface characteristics and all of the changes that occur withing landscapes [4]. Geomorphology dates back to the BC era, when scholars like Xenophanes claimed that the earth's surface had risen and fallen due to fossilized seashells and silt accumulation. Geomorphology has grown significantly in the late twentieth century, incorporating many features of several disciplines like as hydrology, geology, engineering, geographic information systems, and so on [4].

In geomorphology the forces that affect the earth's surface and causes change can be divided into exogenic and endogenic forces where both, exogenic and endogenic forces have an effect on the earth's surface [5]. These two forces can then be separated into many variables based on how they impact the earth's surface. Table 1 shows examples of endogenic and exogenic forces, with tectonic force as an example of endogenic force and fluvial processes, mass wasting, and glaciation as examples of exogenic forces [5].

Table 1. Different factors of geomorphology

<b>Tectonic forces</b>	<b>Tectonic movement/deformation</b>
	earthquakes
<b>Fluvial processes</b>	River formations
	Floodplains
	Precipitation, etc.
<b>Mass wasting</b>	Weathering
	Erosion

	Sedimentation
	Formation of soils, etc.
<b>Glaciation</b>	Mountain/ continental glaciers
	Abrasion, plucking
	formations of moraines etc.,
<b>Human Geomorphology</b>	anthropomorphic activities

In addition, geomorphology can be divided into 4 distinct parts based on study methods which are morphography, morphogenesis, morpho-chronology and morphometry. Each method entails a different way for approaching geomorphology where morphography is classifying landforms based on a qualitative approach and direct observation while morphogenesis and morpho-chronology is focused on origin and age of landforms respectively.

Morphometry, on the other hand, is a mathematical and quantitative approach to evaluating the earth's surface and landforms [7]. In essence, using this geomorphological approach, we may examine the earth's surface and build morphological forms using digital data. Unlike morphography, which takes a lengthy time and involves a field study, this method allows for a more convenient and remote research of geomorphology. The morphometric methods was first developed between 1940 and 1970 during which portions of the data were extrapolated from topographic maps and analyzed with various statistical and morphometric analytical methods. However, many of the functions required for morphometric analysis were integrated in geographical software such as ArcGIS between 1980 and 1990, thanks to the advent of personalized and publicly available computers [4]. For the purposes of this research, we will use TPI based landform and slope classification method developed by Weiss (2001) for analyzing Baganuur landscape and a simple ArcGIS method for analyzing watershed.

- Topographic position index (TPI)

TPI or topographic position index is a morphometric property that denotes the relative topographic position of a point in relation to the mean elevation of its surrounding area within a specified neighborhood [8]. In simplified terms, it assigns a certain positive or negative value to a topographic point based on whether if the point is higher or lower than its surrounding area based on a DEM. With this, an entire area can be arranged into positive or negative values which can then be subdivided into landforms and slope classes based on its value. Figure 1 values area spread over a land where values near zero denote flat slopes and plains while positive values represent hills and ridges with higher. On

the other negative values can either denote depression within a plains or valleys in between mountains and hills [9].

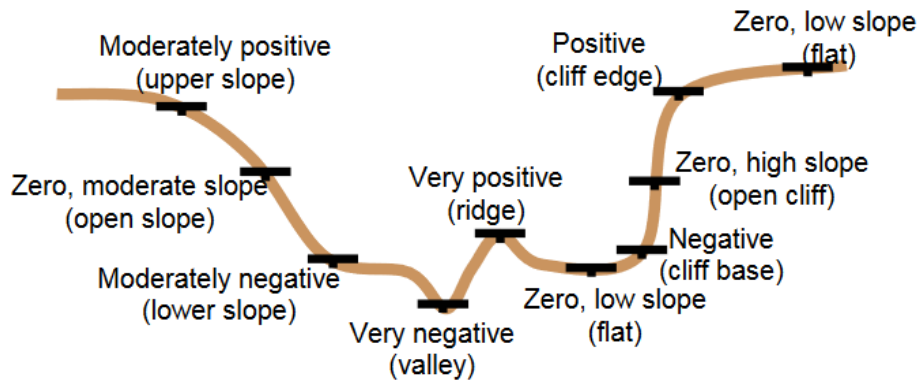


Figure 1. TPI values in relation to slope position (source: Weiss 2001 [9])

The surrounding area from which the TPI value is determined is called the annulus area (Figure 2). The central point of the annulus or in this case the elevation point  $pt$  is compared to the mean elevation of the neighborhood  $u$  which is determined from the grey area of the annulus. If the  $pt$  is higher or lower than the  $u$  the TPI value will be given as positive or negative. Single TPI maps can be used to create a varying degree of slope position classes while landform classes require a combination of two TPI's with a lower and neighborhood size.

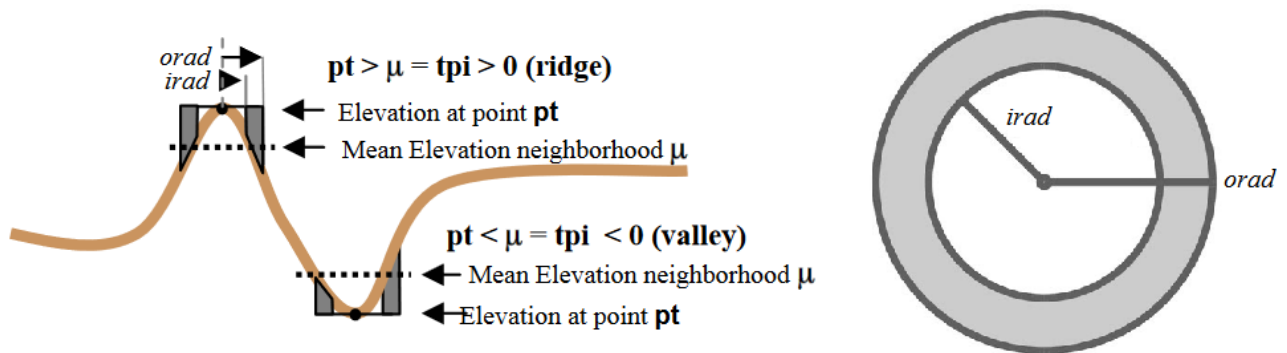
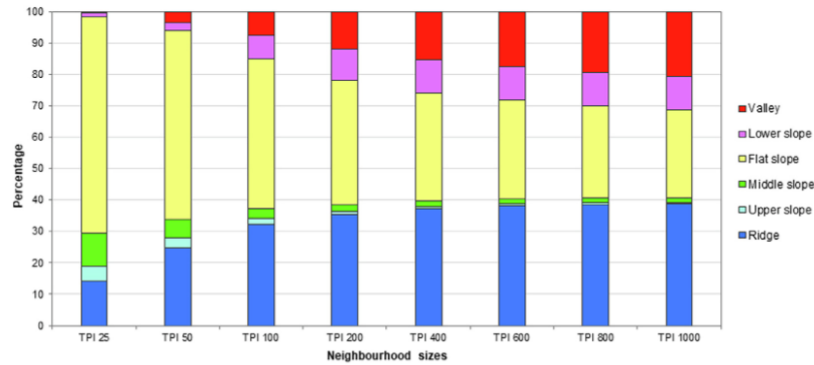


Figure 2. TPI value in relation to its annulus area (source: Weiss 2001 [9])

Since the TPI values are determined by the surrounding annulus area, the radius of the annulus can be altered in order to display specific slope position classes. According to previous studies, TPIs with a larger neighborhood classes were better at detecting flat slopes and broad open plains, while TPIs with a smaller neighborhood class were better at identifying strong and steep slopes, such as ridges and

hills. Graph 1 illustrates the relationship between slope class and neighborhood size in a Himalayan landscape where the percent coverage of valleys and lower slopes increases correspondingly with neighborhood size, whereas the percent coverage of flat slopes, middle slopes, and upper slopes decreases. The ridge cover, on the other hand, appears to level out starting at TPI 400 and does not exceed 40% even at TPI 1000.



Graph 1. Stacked percentages of the slope position classes from different neighborhood classes (source: GIS-based landform and LULC classifications in the Sub-Himalayan Kaljani Basin [40])

- Watershed analysis

A watershed, drainage basin, or catchment area is a land area from which rain and precipitation drains to a single outlet such as rivers, small streams, lakes, or reservoirs. Watersheds are crucial to the environment because they determine the overall health of a river system and, as a result, the surrounding ecology [42]. Watershed are separated by drainage divides and can be sub-divided into ocean basins, river basins and sub-basins depending on its size [10]. Mongolia is divided into three

ocean drainage basins: the Asian Interior basin, the Arctic Ocean basin, and the Pacific Ocean basin, as well as 29 minor river basins that make up the three ocean basins (Figure 3) [11].

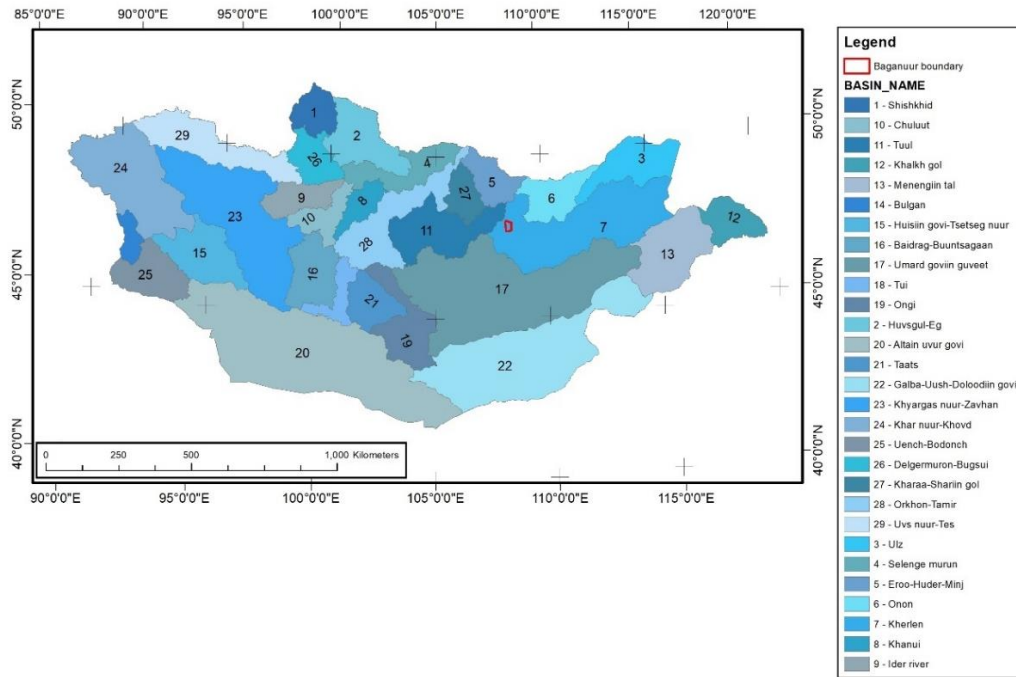
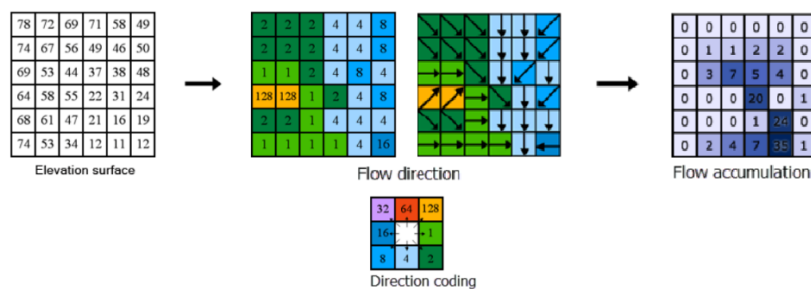


Figure 3. River basins of Mongolia

Using a simple ArcGIS approach, this study will identify the subbasins within the Baganuur region. This method extrapolates watershed areas based on flow accumulation and flow directions computed from a DEM. Flow direction in this instance is derived from elevation differences and is represented as value ranging from 1 to 128 with each value representing a different direction [12]. Flow accumulation however is the added weight of each flow direction cell that is pointed in the same direction (Figure 4). Each instance of direction cell adds more weight to its next cell, eventually forming a complex stream network over a surface [13]. From this stream network or flow accumulation, an outlet point must be manually created from converging stream network over the desired area, in this case Baganuur district.



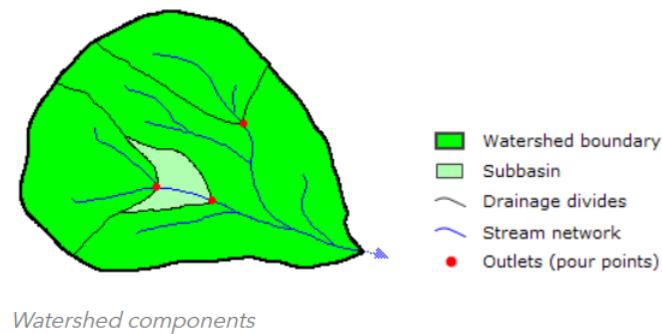


Figure 4. Flow direction, Flow accumulation and watershed components in ArcGIS (source: [12, 13])

## 2.2 Soil Erosion

Erosion is one of the most significant geomorphological processes since basic human requirements such as clean water, clean air, and food are all dependent on healthy soil. Although erosion is a natural process that takes a long time to occur, human activities such as farming, mining, deforestation, overgrazing, and other activities are accelerating erosive processes. This not only reduces soil fertility and other possible uses, but it also has unintended consequences such as increased sedimentation, pollution, and etc. [14]

Erosion is the detachment and transportation of surface level particles caused by erosive agents such as water, wind, gravity, and glacial ice. The most vulnerable materials to erosion are residual products of weathering and any type of consolidated deposits or loose soils. Furthermore, depending on the geography and the source of the process, erosion might be characterized as rill, sheet, or gully erosion. When quantified, erosion is expressed as unit mass or volume per unit area and time, but in most cases, it is expressed as tonnes of mass per hectare and year.

On a global scale, Asia was found to have the third highest average erosion rate after South America and Africa in 2012. At a localized scale, Mongolia was estimated to have a much lower erosion rate compared to other Asian countries with an estimated average erosion rate of 0-1 (metric tons\*ha<sup>-1</sup>\*year<sup>-1</sup>) for a majority of its area with some higher degree of erosion in its western regions which appears to range between 3-5 and 5-10 in certain areas (Figure 5) [35].

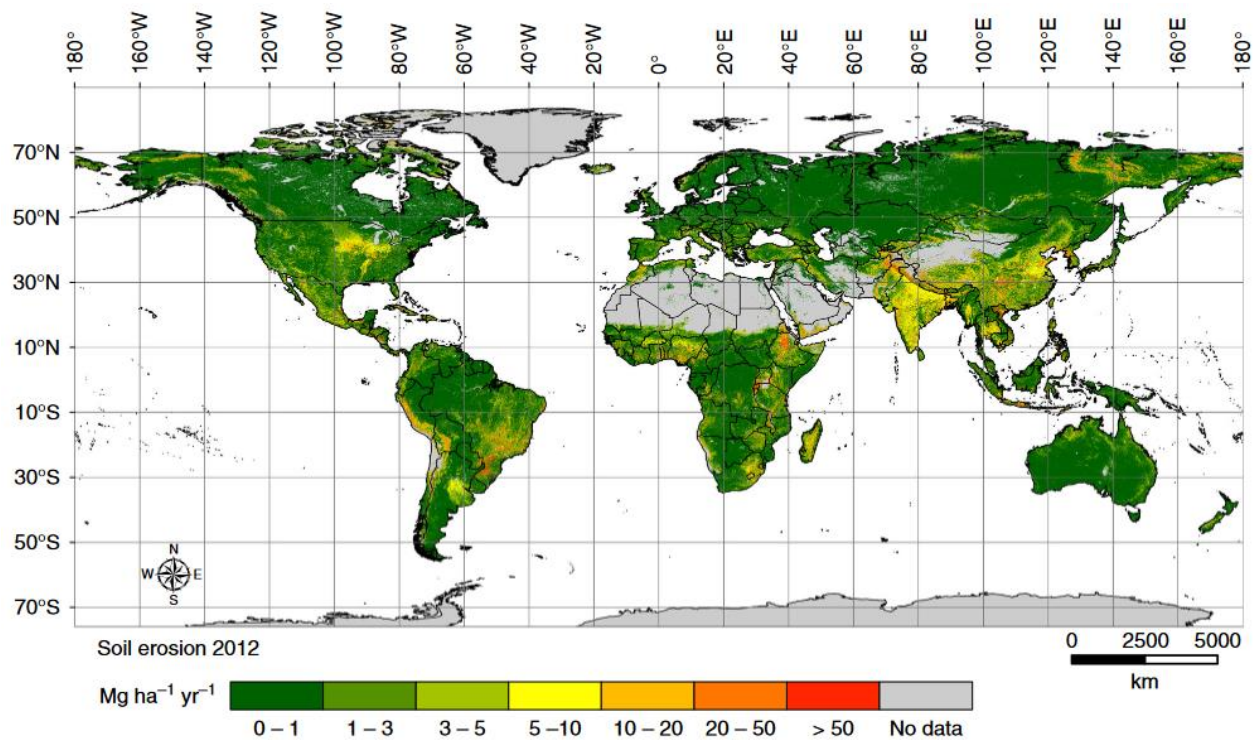


Figure 5. Global soil erosion rate of 2012 (Source: An assessment of the global impact of 21<sup>st</sup> century land use and change on soil erosion [35])

However, from an erosion study specifically conducted within Mongolia, the region was estimated to have an average soil loss between 0-3 tonnes\*ha\*year and 0-1 tonnes\*ha\*year on its western and eastern sides respectively. Additionally, the average soil loss around the central Mongolian steppe areas had an average erosion of 5.613 tonnes\*ha\*year in 2013. In terms of cropland and agricultural erosions, studies indicate that average erosion ranged between 32.6 and 49.6 tonnes\*ha\*year. [14]

### 2.2.1 Effects of vegetation and rainfall

In terms of the amount of sediment removed from the lands surface, erosion through water is the most important type as it has the greatest effect. Materials eroded from slopes due to runoff and rainfall are transported via streams to nearby lakes and oceans.

During the early stages of rainfall, most of the precipitation infiltrates into the ground. However, if the rainfall is strong and/ or long enough it creates a saturated zone just under the soils surface. Eventually when the ponded water level exceeds surface irregularities, it causes a thin layer of water to flow over the surface level downslope. This phenomenon is known as overland flow and is responsible for causing

sheet erosion. This eventually leads way to rill erosion which eventually after a certain period of time forms gullies that gradually extends upstream [16].

The amount of erosion occurring on slopes is a complex phenomenon which depends on functions such as climate, topography, rock type and vegetation. For example, even though a desert region has poor surface soil qualities, it is very unlikely that much erosion through overland runoff will occur there because of the low amount of precipitation. In addition, regions with high vegetation density, erosion is also low due to the additional support of soils by vegetation [17].

In contrast, sediment yield is typically at its highest if the area is semi-arid and has irregular or scarce rain that causes high runoff as seen in Figure 6 [18]. This graph demonstrates a very simplified relationship between rainfall, vegetation and sediment yield and is based on a continental climate.

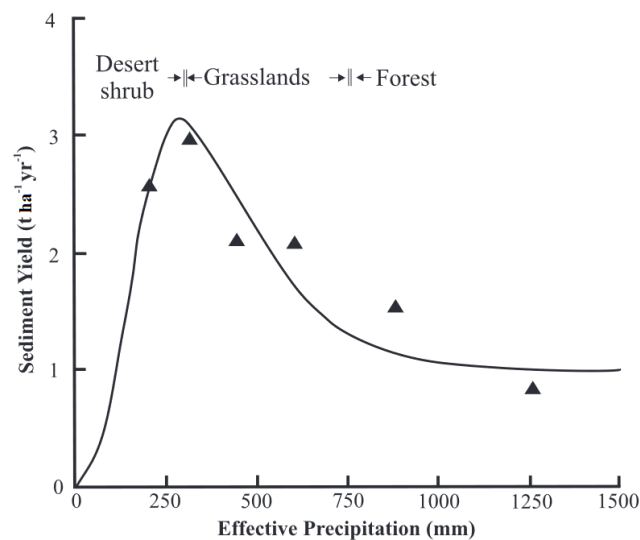


Figure 6. Relationship between Effective precipitation and Sediment yield in USA (source: Dynamics Interactions of Life and its Landscapes [18])

### 2.2.2 Effect of wind

Another major source of erosion is wind. Although wind erosion is less predominant than erosion via water, it can still be a major source of erosion depending on the geological properties of the region. Erosion via wind can be generalized into two types, which are deflation and wind abrasion. Deflation a process where loose and usually fine-grained sediments are removed due to wind. This phenomenon is likely to occur if the soil lacks any form of protective cover such as vegetation and large sediments. Wind abrasion on the other hand is the result of sediments carried by wind colliding with large solids and wearing them down. [17]

Wind erosion potential is proportional to wind velocity and particle size distribution on a soil's surface. Because different particle sizes have varying physical qualities, the critical shear velocity (the velocity necessary to dislodge a particle from soil) varies [14]. The critical velocity is shown to be at its lowest when particle sizes are between 75 and 250 micrometers and increases as particle size falls or increases outside of this range, as illustrated in graph 1. Although it is generally known that smaller particles are simpler to remove, particles smaller than 50 micrometers (silt and clay) are more difficult to remove due to their cohesive and compact nature (Figure 7).

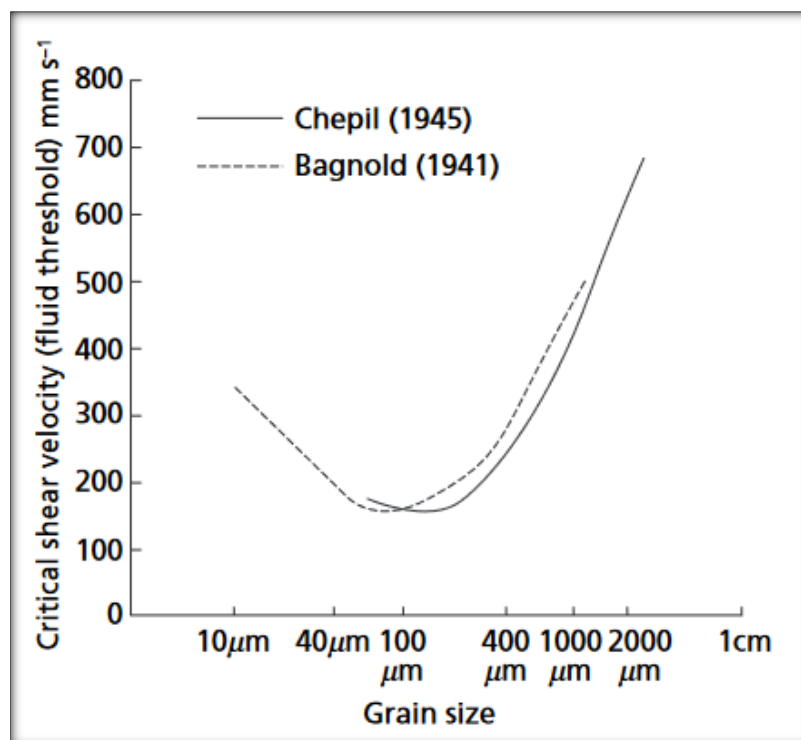


Figure 7. Relationship between critical shear velocity and grain size. (source: Soil erosion and conservation [14])

While precipitation and, by extension, runoff have a direct impact on erosion via water, a lack of precipitation can make soils more vulnerable to wind erosion due to drought and lack of vegetation growth [19]. As a result, semi-arid and dry regions with annual precipitation of less than 500mm and 250mm, respectively, as well as desert areas like Mongolia's Gobi, are particularly prone to wind erosion.

A previous study conducted in both Mongolia and Inner Mongolia used the FCM or Fuzzy c-means method to assess wind erosion risk. This study uses a combination of 4 main factors to create 5 different classes of wind erosion risk. These 4 factors are average relief degree of land surface, soil dryness, intensity of wind energy and vegetation coverage.

The result of this assessment is presented in (Figure 8), which shows that majority of Mongolia's northern region is at slight or no risk of wind erosion. Wind erosion, on the other hand, begins to intensify further south, with the mid-section of Mongolia experiencing moderate wind erosion and the southern regions experiencing intense or severe wind erosion. The extreme wind erosion can be seen in parts of the provinces of Govi-Altay, Bayanhongor, and Umnugovi. From this mapping, it could also be speculated that the Baganuur area is under a slight risk of wind erosion.

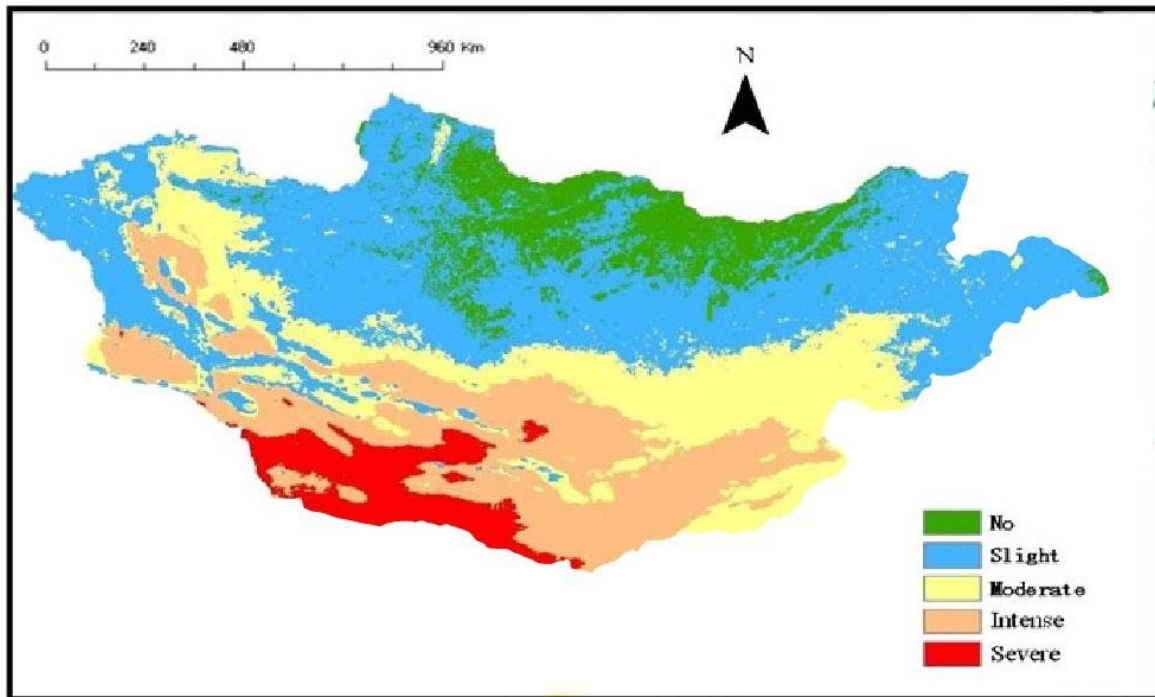


Figure 8. Wind erosion hazard map of Mongolia. (source: Wind erosion hazard assessment of the Mongolian Plateau using FCM and GIS techniques [36])

### 2.2.3 Anthropomorphic influence

Human activities otherwise known as anthropomorphic activities has become a major factor in land use and change due to increasing world population and the need to support their needs. As a result, natural processes that would naturally occur over a long period of time is being accelerated to a worrying degree. One such phenomenon that is affected in this manner is soil erosion.

As stated before, soil erosion is affected by a myriad of different factors such as topography, vegetation, climate, rainfall etc. However, due to anthropogenic influences all of these factors are affected both directly and indirectly. For example, the development of major settlements and transportation routes modify surface runoff altering water erosion [20]. A broad and simplified overview of the direct and

indirect effects of anthropogenic activities on geological features can be seen in (Figure 9). For Mongolia, there are several major factors that are affecting land degradation and soil erosion.

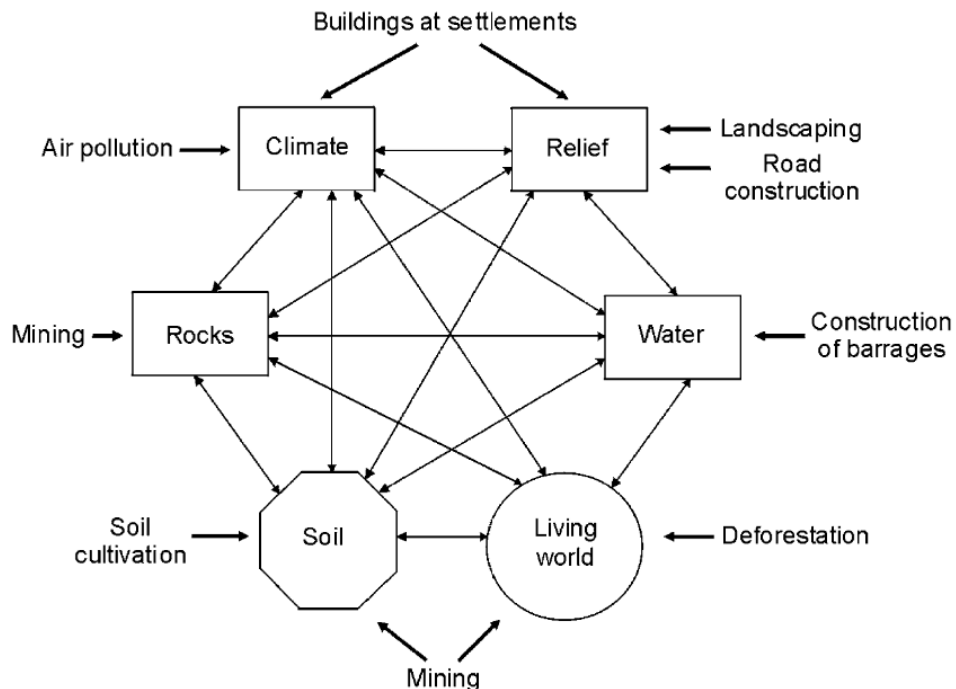
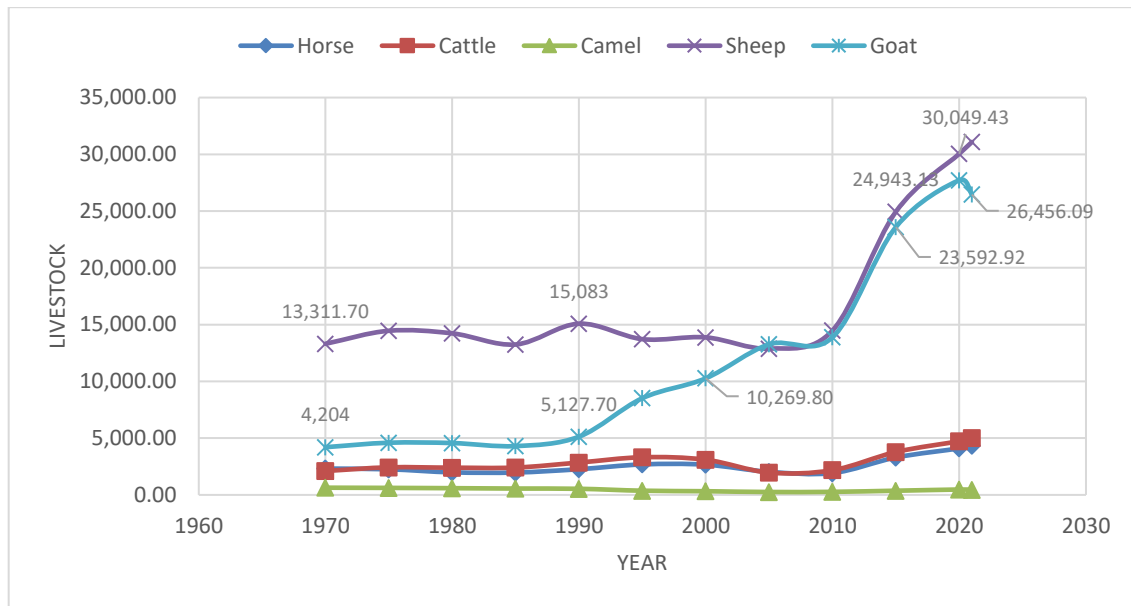


Figure 9. Typical impact points of the physical and geographical system and anthropogenic activities (source: anthropomorphic Geology [20])

- **Overgrazing**

Mongolia's overgrazing of pasturelands and degradation is becoming a severe problem as the country's livestock population grows. While the number of large livestock such as cattle, camels and horses has not increased significantly in recent decades, the number of sheep and goat has nearly tripled since 2005. (Graph 2). The increased demand for cashmere products is largely to blame for the increase in small livestock. And, unlike most other animals, goats eat not only grass but also the roots of plants, which exaggerate the problem of pastureland degradation. While the role of livestock

in soil degradation is well-known, it is difficult to estimate the exact number of areas affected in this way due to its complexity [15].



Graph 2. Total livestock count of Mongolia between 1960 and 2021 with a five-year interval (source: [39])

- **Road and transportation**

Land degradation in Mongolia is also influenced by transportation and roads. According to estimates, there was roughly 49'249.9 km of automobile roadways in 2010 which included intensively used main roads and less used off roads. Only 6.72 percent (3'174.8 km) of them were hard concrete roads, while 7.84 percent (3704.7 km) were improved gravel roads, with the remainder being dirt roads. These dirt roads are formed not only by the transit and daily activities of ordinary people, but also by the passage of heavy machinery and carriers from mining sites [15]. Such transportation and transit on dirt roads are not only a cause of dust generation, but it also destroys the vegetation and causes the soil to compact reducing its water infiltration. Dirt roads that have been used for a prolonged amount of time can eventually turn into gully erosions which grow over time [21]. In addition, because it takes a long period of time (roughly 10-15 years) for vegetation to fully recover on such pathways, dirt roads are also one of the leading causes for desertification in Mongolia. Different studies carried out in 2006 and 2010 estimated that roughly 7000 km<sup>2</sup> land was degraded due to roads of which 3260 km<sup>2</sup> is located on main transit roads. [21].

- **Effect of mines**

Mining activities can modify the environment in a number of ways depending on the type of mine itself. Even though underground mines are much less apparent and disturb a significantly smaller area of the ground's surface, both underground and surface mines have their own specific challenges when it comes to environmental pollution and safety control.

Surface mines can be divided into open-pit or strip mining where open pit is used when the ore body is located near the surface as a three-dimensional body. On the other hand, strip mining is more commonly used when the desired ore exists as a layer near and parallel to the surface. Both methods remove a large portion of the overlying vegetation, soil and rock and then dump them as spoil banks. The exposed materials may immediately start to go under chemical and physical weathering depending on the nature of the materials [17]. This could have a severe impact on the surrounding environment as eroded material from waste tips could eventually be transported over the surrounding soil and eventually into streams and lakes. However, from satellite imagery and field observations, the Baganuur coal mine has protective perimeter dirt piles throughout its eastern side which helps to prevent sediment washing (Figure 10).



Figure 10. Dirt piles used to prevent sediment washing from the Baganuur mines waste tips.

### 2.3 Revised Universal Soil Loss Equation (RUSLE)

Universal Soil loss equation otherwise known as USLE was originally developed by W. H. Wischmeier, D. D. Smith and others with the U.S. Department of Agriculture, Purdue university and other environmental faculties with the purpose of calculating soil loss from agricultural areas. This method uses rainfall, soil erodibility, slope length, slope steepness, cropping and conservation factors in order to estimate soil loss. However, because USLE was designed for agricultural lands with gentle slopes, it was unsuitable for more complex areas with varying topographic features and steeper slopes.

In order to use the USLE method for different circumstances, it was modified into the revised universal soils loss equation (RUSLE). The new version of the USLE improved on its predecessor and allowed for soil loss calculations in areas with more complex topographic features [22]. RUSLE equation consists of 5 factors which encapsulate almost all of the major factors that are relevant to soil erosion, these factors are rainfall erosivity, soil erodibility, topographic steepness, land cover and management and conservation practices. RUSLE equation is represented as:

$$A = R * K * LS * C * P \quad (1)$$

Table 2. RUSLE factors

1	Topographic steepness	LS	$LS = (\chi * \lambda / 22.13)^{0.4}$ $* (\sin\beta / 0.0896)^{1.3}$
			X: Flow accumulation
			l: raster cell dimension
			b: Slope inclination in degrees
2	Rainfall erosivity factor	R	$R = -8.12 + (0.562 * P)$
3	Soil erodibility factor	K	Sand = 0.16, Loamy sand = 0.12, Sandy loam = 0.2
			or
			$K_{USLE} = F_{csand} * f_{cl-si} * f_{orgc} * f_{hisand}$
4	Land cover and management factor	C	$C = (-NDVI + 1) / 2$
5	Conservation practice	P	P factor ranges from 0 to 1
			If high quality preservation practice P=0
			If low quality conservation factor P=1

Topographic steepness (LS), rainfall erosivity (R) and soil erodibility (K) factors are typically constant and do not change when conservation practices are placed since these are inherent to the landscape [22]. Land cover and management factor (C) is dependent vegetation growth and density while conservation practice (P) is purely dependent on human influence on the landscape.

Calculating and determining each RUSLE factor can differ substantially from region to region as different climatic conditions, soil properties, vegetation growth, slope and land usage affect the result of each factor and RUSLE as a whole. As a result, different sets of equations and methods for calculating RUSLE and its factors are used by research depending on the region RUSLE is applied to [22].

## 2.4 Corona Satellite images

Ran between 1960-1972, the CORONA program was designed to take a series of topographic images by the collaborative efforts of the U.S. Air force, Central Intelligence Agency (CIA) and some additional private agencies. The U.S. first initialized the program with the purpose of gathering intel on foreign countries after their U2 espionage aircrafts were destroyed. With over several thousands of images taken, the CORONA satellite images remained classified until 1995 when it was made public by the 42<sup>nd</sup> president of the U.S. Bill Clinton [23].

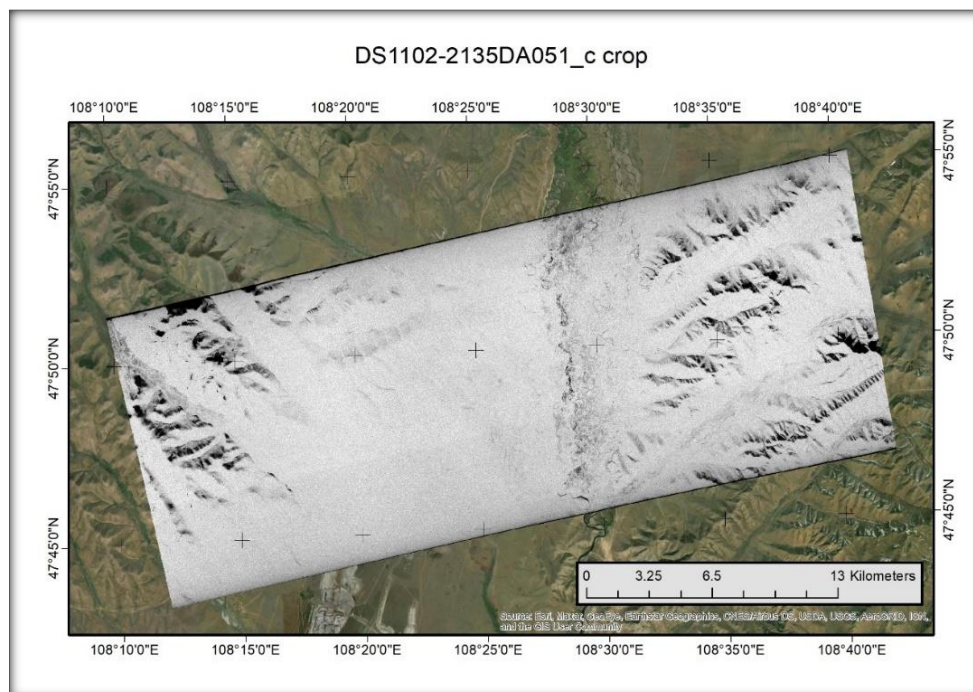


Figure 11. CORONA satellite imagery example

Because Landsat-TM and other similar sensors date back only as far as 1972, CORONA satellite imageries provide vital information of landscape and use before that this period. However, because CORONA images have no spatial references and coordinates, this research will take an in depth look into how CORONA images are georeferenced and applied to real world imagery. The resulting images will be used as a comparison with present day satellite images to determine the change in landscape and the development of the Baganuur coal mine.

## 2.5 Area of Study

Baganuur is one of Ulaanbaatar's outlying districts, located around 130 kilometers east of the capital city. It is made up of four khoros and covers an area of about 620 square kilometers. Baganuur has a total population of 29233 people and 8557 households as of January 2022 [1].

The majority of Baganuur district is made up of grassy plains, with small hilly mountains to the west and east of the region. In addition, the district's eastern border is marked by the Kherlen River, which serves as a natural barrier. The mining hole is the lowest point of the grassy plain, which is at 1290m. The area's highest point is 1795 meters above sea level. The plains between 1300 and 1400 meters are home to all of the villages, ger areas, mining sites, and small patches of cropland (Figure 12).

Baganuur coal mine was first developed in 1978 and currently has an estimated production capacity of 4 million tons per year. Currently it supplies brown coal to 2<sup>nd</sup>, 3<sup>rd</sup> and 4<sup>th</sup> thermal powerplants in Ulaanbaatar, Erdenet and Darkhan thermal powerplants and several other small thermal plants throughout the country [2]. The mine itself consists of multiple mining pits, offices and other infrastructures [3].

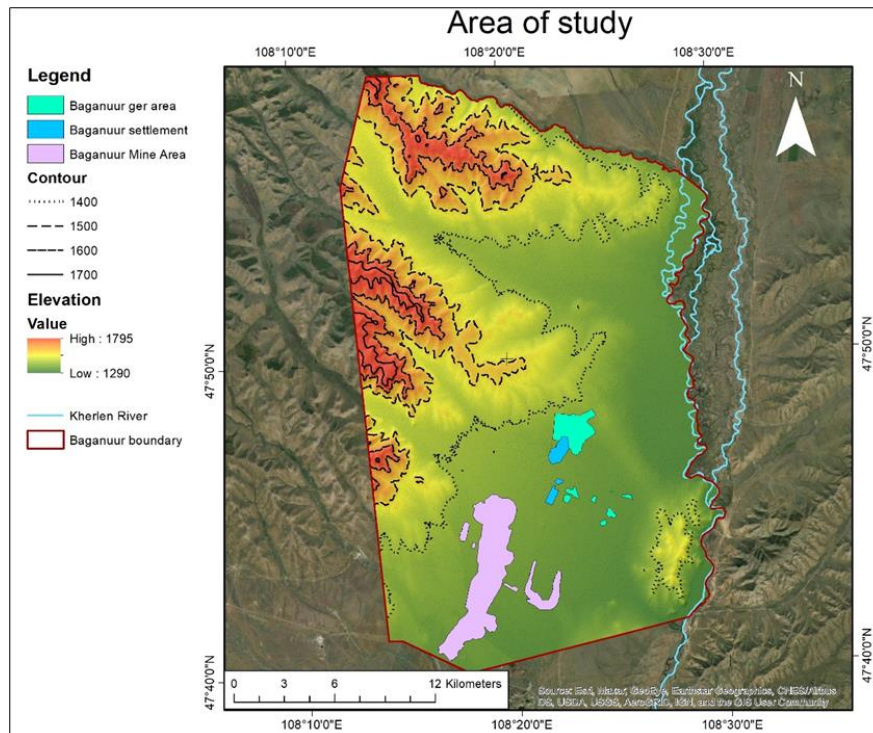


Figure 12. Area of study

## 2.5.1 Soil & Vegetation

The Baganuur region is located in a mountain forest steppe zone, with approximately 31 different types of vegetation where most species seem to be semi drought resistant and drought resistant [24]. The most common types of vegetation appear to be *Festuca* plants and shrubs which covers a majority of the plain. The stony *Festuca* and wormwood herbs fill the mountainous sections, while the riverside area is covered in a mix of willow groves, herb grass, and marshy sedge bent herbs. Larch, birch, and spruce trees make up the majority of the trees found in the Baganuur region (Figure 13).

With the exception of the riverside area, which is made up of alluvial soils, practically all of the area is made up of dark chestnut and mountain dark chestnuts in terms of soil. The Baganuur region can also be categorized into two soil types, Lithosols and Kastanozems, according to the FAO global digital soil map.

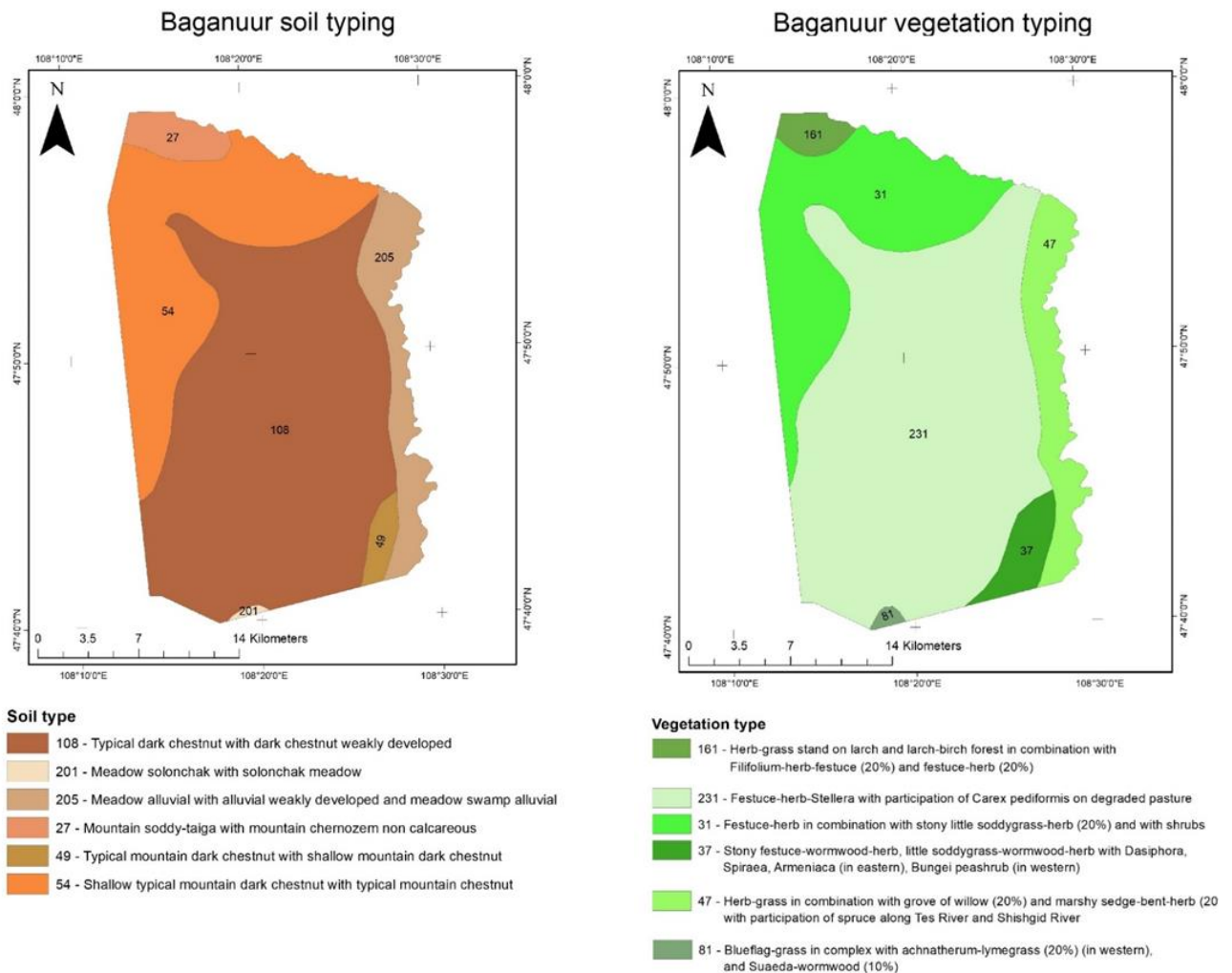
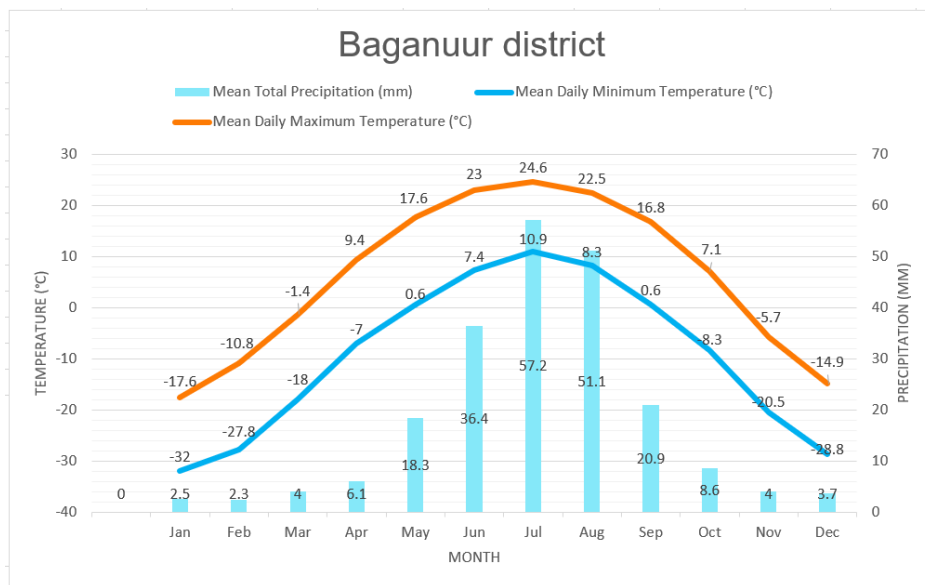


Figure 13. Baganuur area soil and vegetation typing (source: [41])

## 2.5.2 Climate

Mongolian climate is characterized by four alternating seasons, a significant degree of seasonal fluctuation in minimum and maximum temperatures, and minimal amount of rainfall. Annual precipitation fluctuates between 200 and 220 mm on average, with the Gobi region receiving only 38.4 mm on average [25]. Annual temperatures in the northern mountainous parts range from -4 to -8 degrees Celsius, 2 degrees Celsius in the dessert-steppe region, and 6 degrees Celsius in the southern desert region, where it borders with China [37].

The yearly precipitation in Baganuur is predicted to be 215.2 mm with a potential evaporation of 508 mm\*yr<sup>-1</sup>, making it a semi-arid region with an average annual temperature of -1.83 degrees Celsius. The majority of the precipitation falls between June and August (67.21 mm), with a peak of 57.2 mm in July. The smallest quantity of precipitation, 2.5 mm, was recorded in January (Graph 3). The highest temperature is 10.9 to 24.6 degrees Celsius, while the lowest temperature is -32 to -17.6 degrees Celsius [38].



Graph 3. Baganuur district temperature and precipitation graph (source: [38])

### 3 Methodology

#### 3.1 Georeferencing Corona Satellite imagery

CORONA satellite imageries offer a great resolution of the mid to late 20'th century. However, since these images were taken with a panoramic camera, they virtually have no coordinate systems or control points assigned to them which makes it much more difficult to use these high value images without georeferencing and editing for other projects. This section of the paper describes how CORONA images are georeferenced using the ArcMap's software and which errors to avoid.

##### 3.1.1 Georeferencing process

- Step 1: Loading CORONA satellite image into ArcMap's

Because CORONA satellite images do not have coordinate references, when they are loaded into ArcMap's or any other geospatial processing programs, they will be initially loaded into a random location and not the desired area of study. In order to place the image closer to our desired area we use the **Fit to Display** command shown in Figure 14, Figure 15.

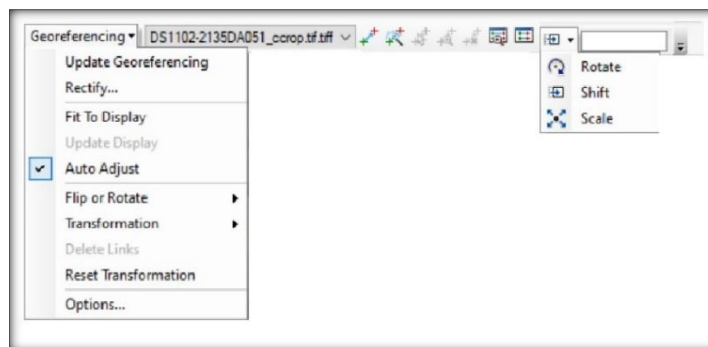


Figure 14. Georeferencing menu

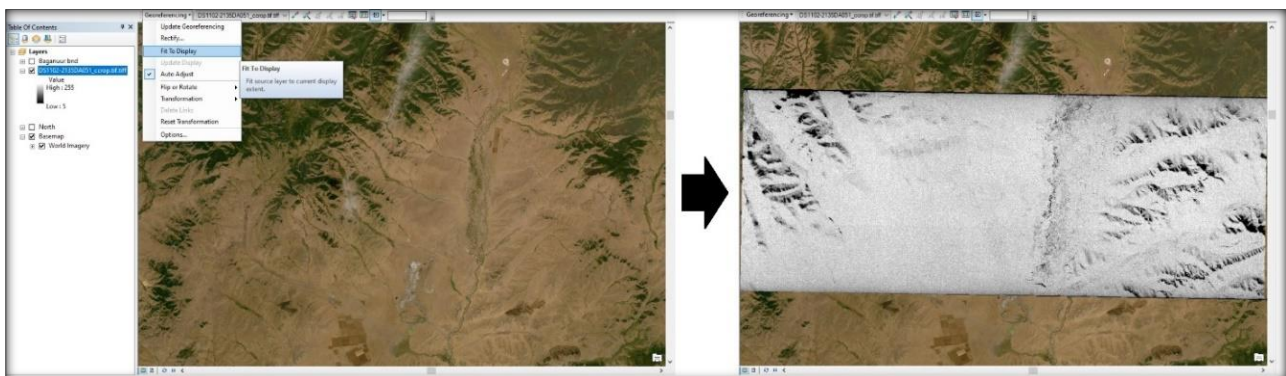


Figure 15. Georeferencing: Fit to Display command

- Step 2: Adjusting CORONA images to the background

After the image has been integrated to a suitable location using **Fit to Display**, it can now be adjusted using the **rotate, shift and scale** functions (Figure 14). The purpose of this step is to find an approximate area where the CORONA image would fit into when overlaid with the background image. While doing so, it is better to work with the CORONA image slightly bigger than the background topography so that the details of both images can be better compared. After finding the intended location (Figure 16), shift the CORONA image to the side for linking process.

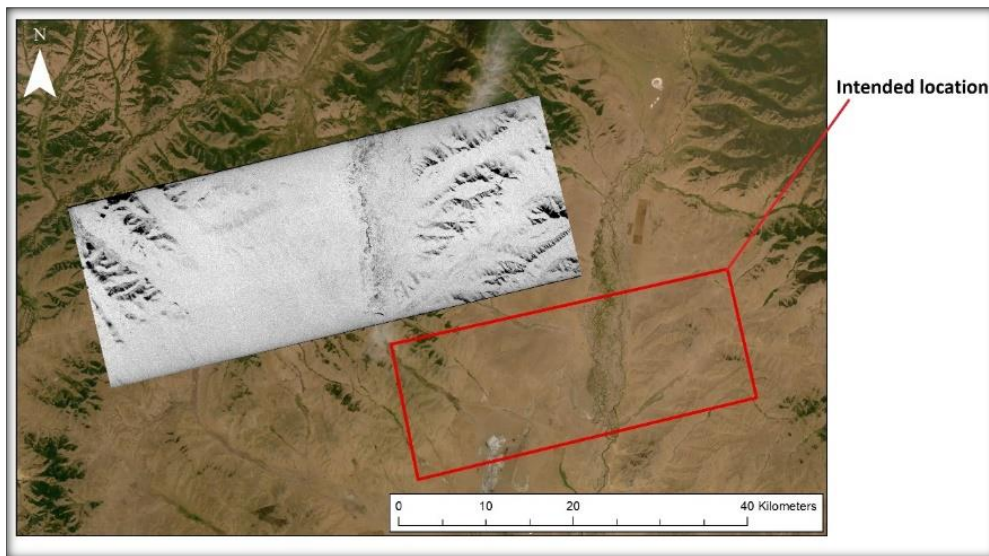


Figure 16. Georeferencing intended location...

- Step 3: Adding control points

In order to add control points, we first need to open the **Link Table** shown in Figure 17. When the link table is opened it will initially be empty and have only 1 option for a transformation. However, after a certain number of control points have been added to the images the program will automatically allow for different transformation options to be used.

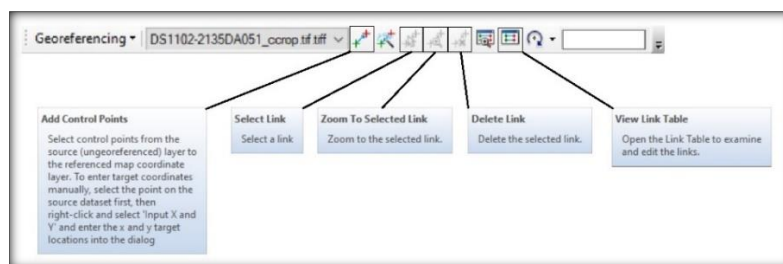


Figure 17, Georeferencing menu: Add Control Points, Select Link, Zoom to Selected Link, Delete Link, View Link Table

After the link table has been opened, it is now important to carefully compare the CORONA satellite image and the base map in order to find a feature that can easily be identified on both images. Such features could be large rock formations, mountain summits, peaks, ridges, intersections, river curves and human structures such as settlement, bridges and other structures. It is important to note however that due to the great time difference between the CORONA satellite image and current day, some human structures have been demolished and/ or relocated to left in ruin. Therefore, it is necessary to ensure that the control points used are reliable.

When the **Add control point** command is used, it will create two distinct markers (Figure 18 A, B). The green marker which appears when a control point is added to the CORONA satellite image is called a **source control point**. On the other hand, the red marker appears when the control point is applied to the reference image which in our case is the world map and is named **Ground control point**. These two control points combined will designate where the CORONA satellite image is to be located on the real map. When the first control point is added, the ground and source control points will overlap perfectly. After a few more control points are added, the source and ground control points begin to diverge (Figure 18 - C) due to the distortion of the CORONA images.

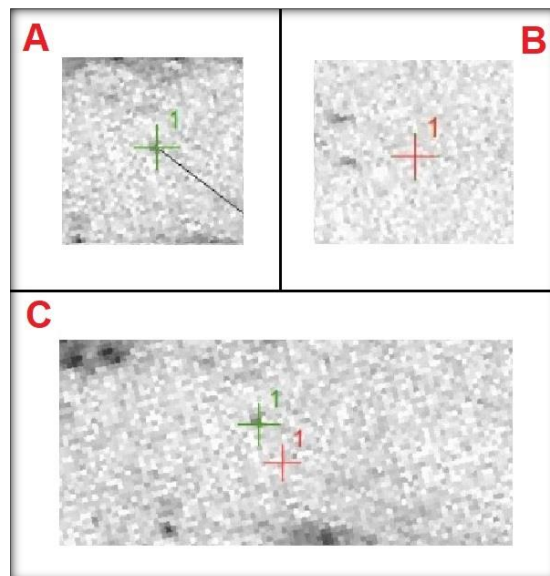


Figure 18. A: Source control points, B: Ground Control Points

- Step 4: Mosaicking

After each strip of CORONA image has been properly georeferenced, they need to be mosaicked in order to create a singular cohesive image. Mosaicking is accomplished by using the **image analysis** tool of ArcMap's (Figure 19).

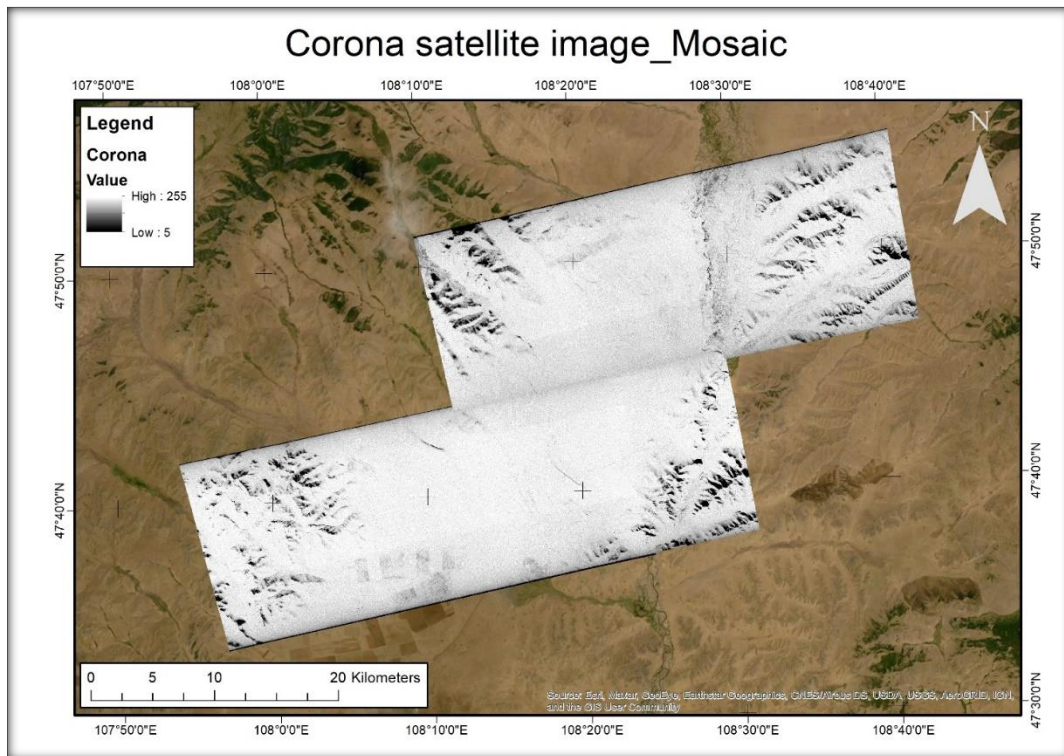


Figure 19. Mosaicked CORONA satellite imagery

### 3.1.2 Transformations

After a sufficient number of control points/links have been added to the raster image, we can use the transform or warp the raster image to permanently match the map coordinates of the target data. In the ArcMap's systems there are polynomial, spline and adjust transformation settings which can be used to correct different levels of distortions.

Lower order polynomial transformations generally allow for small scale alteration and are generally better for images that have small scale distortions. As shown in (Figure 20), first degree polynomial transformation allows for almost no degree of warping and bending while the second- and third-degree transformation allows for an increasing level of modifications.

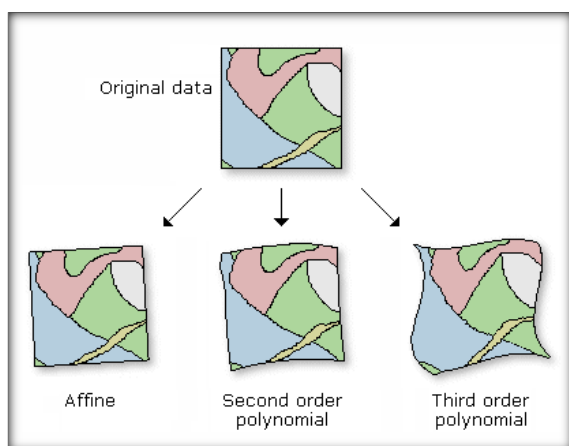


Figure 20. ArcMap's Polynomial transformations (source: [])

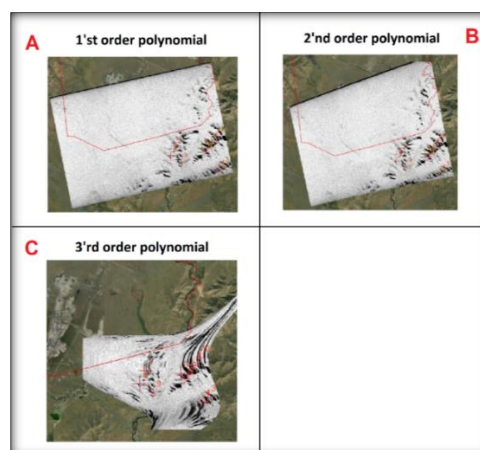


Figure 21. Example of 1'st, 2'nd and 3'rd order transformations on a georeferenced image with unevenly distributed control points

However, lower order polynomial transformations are unable to correct images with the level of distortion shown in (Figure 21), thus non-linear rubber sheeting transformation was used. For the case of ArcMap's transformations, the **Spline** transformation is regarded as a true rubber sheeting that is optimal for local but not global accuracy [27]. However, it should also be noted that the **rubber sheeting** or **Spline** methods should be used with care due to its high dependency on control points. The spline transformation matches the source control points directly to the ground control points regardless of spacing and geometry of other control points. This means that distances between control points are not guaranteed to match the background if the control points are not evenly distributed.

### 3.1.3 Technical limitations of CORONA images

Since these images were taken using panoramic cameras, they exhibit a high amount of geometric distortion along with some brightness variations. Because of this, CORONA images had large radial distortions that increased with distance from the center of the image. Moreover, cropped sections of CORONA images used for localized areas could potentially have different forms of distortions depending on the area of the map. For example, in (Figure 22) the green crosses represent the control points placed on the CORONA image while the red crosses represent the control points anchored to the reference/background image. When transformed using the polynomial 1 option in georeferencing, we can observe that the CORONA image has different distortion directions along its horizontal and vertical axis. Horizontally, the image is compressed to the center while vertically it is stretched outwards creating a unique distortion. These types of distortions as later seen in section **Transformations**, cannot be corrected using lower order polynomial transformations.

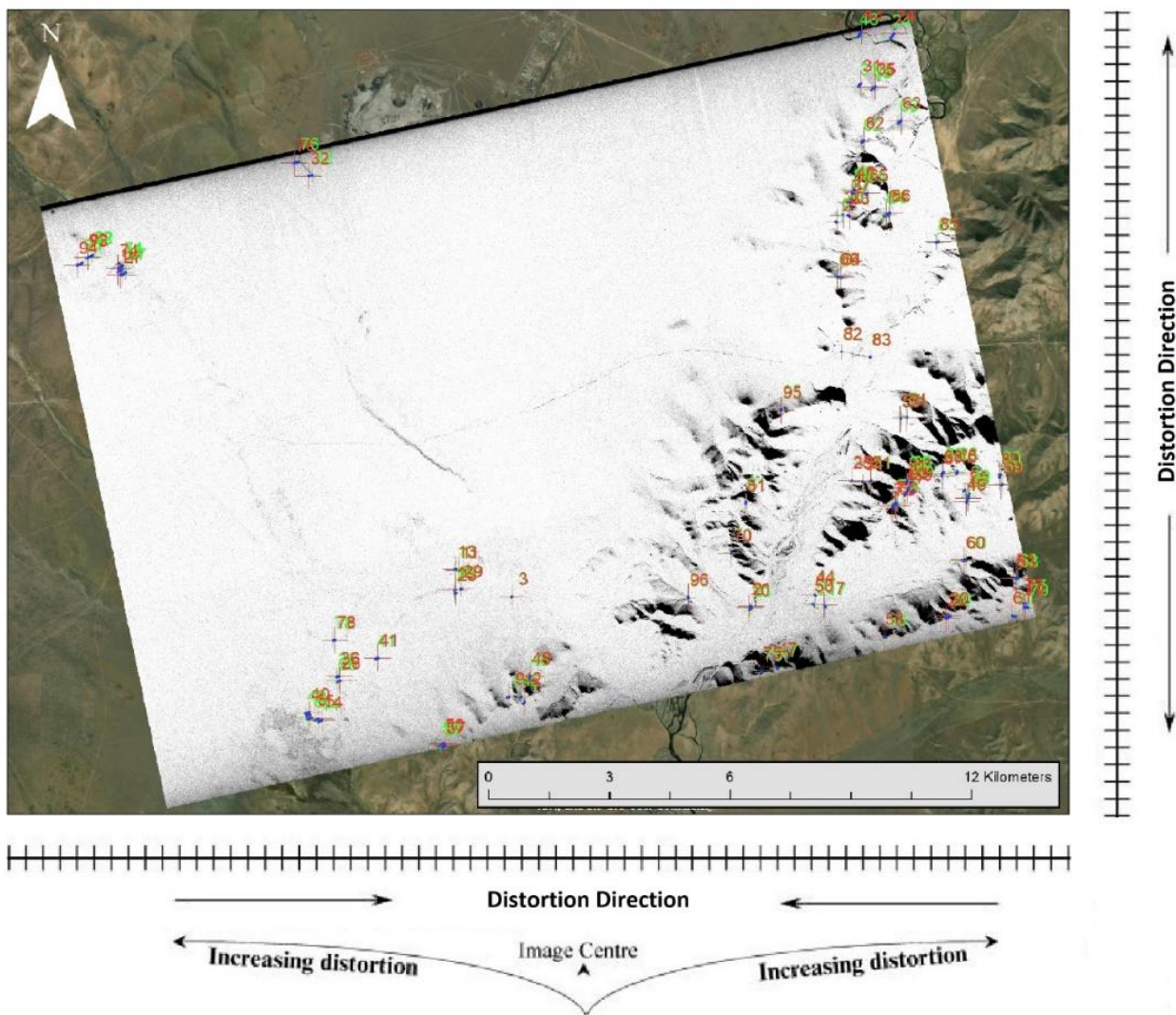


Figure 22. Distortion of CORONA satellite imagery

This creates the need to use higher order transformation methods such as rubber sheeting in order to rectify the distortions. This creates the need for a significantly larger quantity of control points spread evenly throughout the image, increasing the amount of work needed to process a single CORONA image to be usable for other projects.

Another issue that is also present in the CORONA images are related to lighting and shadow. Most images have, blurring, edge darkening, and brightness variations due to the increasing obliqueness of the satellites angle from the nadir. For example, (Figure 23) displays CORONA imagery and world imagery of the same mountain near the north-east of Baganuur. When both images are compared, we can see the shadow created by the CORONA image.

Not only does this make some features and or portions of the CORONA image unusable when georeferencing, it also creates the additional need to manually adjust the color balance and before mosaicking multiple images.

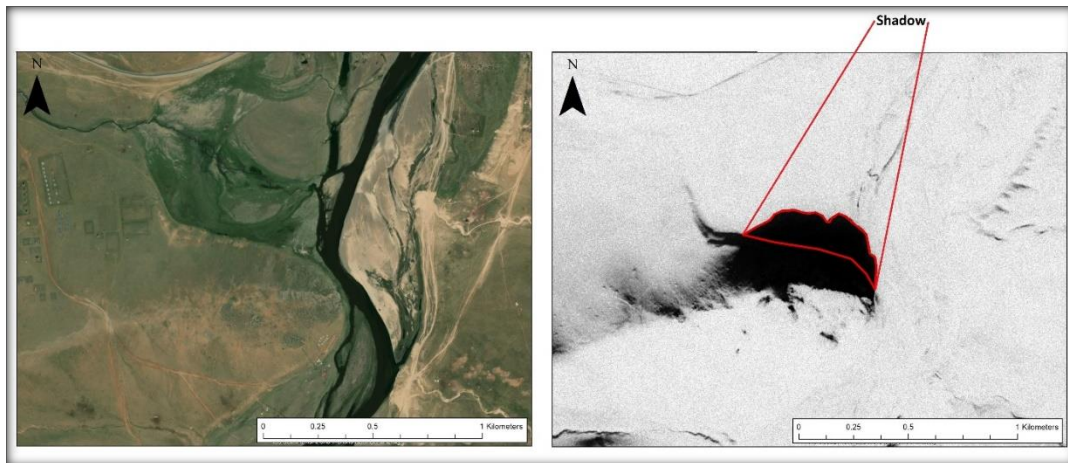


Figure 23. Shadow developed by the CORONA image

In addition, because CORONA images do not contain any real digital data (DEM, infrared, etc), they can only be used for visual comparison. Although there are separate methods of creating high resolution DEM's from CORONA images using alternative software's, a more detailed discussion of these methods is beyond the scope of this paper

### 3.2 RUSLE Calculations

The RUSLE equation is dependent on multiple factors which can be either obtained from satellite imagery or extensive field study. For this thesis, rainfall erosivity, land cover management, topographic and topographic steepness factors are determined using satellite imagery data as shown in Figure 24. While value for conservation practice is taken from Enkhjargal (2022), soil erodibility factor is determined via two different methods. One value is determined by fieldwork and identifying the soil properties of the study area (Enkhjargal 2022) while the other value is determined by calculating for the FAO global soil classification data using Williams (1995) equation.

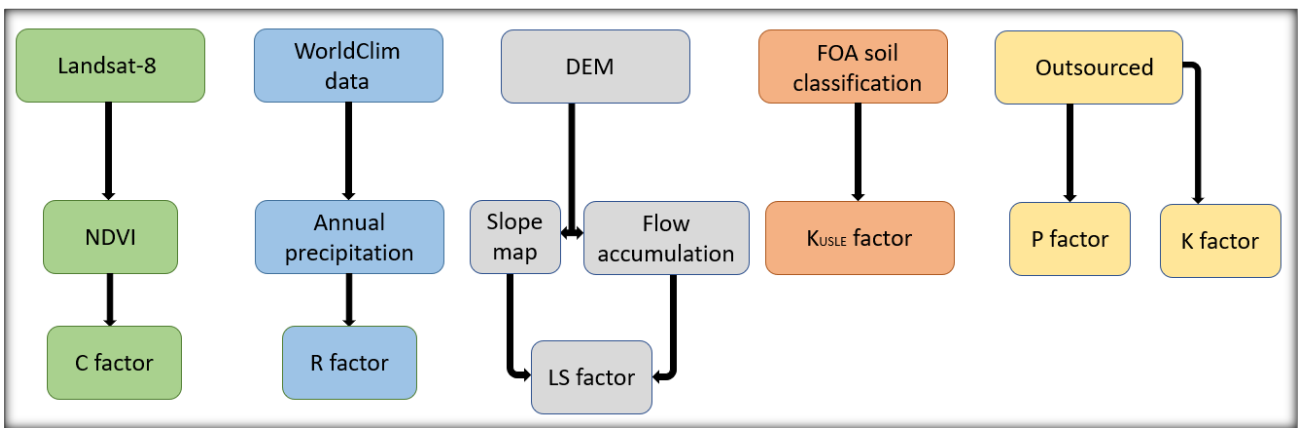


Figure 24. Data sources for each RUSLE factor

#### 3.2.1 Rainfall erosivity (R factor)

R factor represents the erosivity of a certain location due to rainfall and climate. It is typically determined by average sum of the erosivity of storms which is composed of kinetic energy of rainfalls and the maximum 30-minute intensity of storms in mm per hour. However, because kinetic energy and rainfall intensity data of Baganuur is unavailable to us, we will be calculating R factor directly from a raster format annual precipitation data using an equation given by Hurni-1985 as suggested by a previous study of [28]. The equation is given as

$$R = -8.12 + (0.562 + P) \quad (2)$$

where P is average annual precipitation in [mm\*year<sup>-1</sup>] and R is rainfall erosivity in [MJ\*mm\*hour<sup>-1</sup>\*ha<sup>-1</sup>\*year<sup>-1</sup>]. Precipitation data is collected from the WorldClim data website, which offers a wide range of high special resolution global weather and climate data. For this research we will be using the monthly

rainfall data of 2018. In order to calculate the average annual rainfall and R factor. However, because the WorldClim precipitation data covers the entire globe, it first needs to be **clipped** using the **arc toolbox** and turned into a point data as shown in Figure 25.

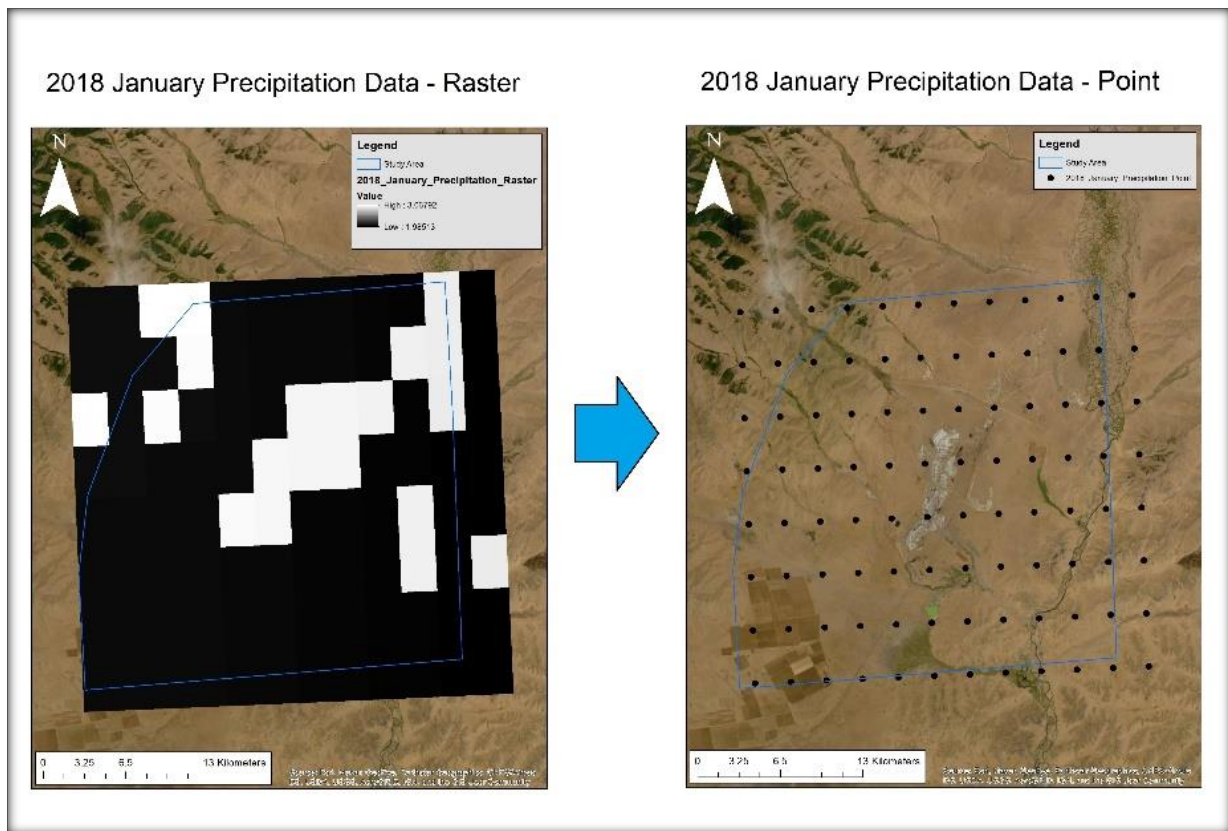


Figure 25. Raster to points transformation example

After each monthly rainfall data has been transformed into point data and then extracted into an excel sheet, annual rainfall data can be calculated and then re-integrated back to ArcGIS as point data. This annual rainfall can then be transformed into raster format using the **IDW** tool from **Spatial analyst tool**. This results in a raster annual precipitation data as shown in Figure 26 - A. Calculating R factor using the **Raster calculator** function from **Spatial Analyst Tools** with the aforementioned equation results in a R factor shown in Figure 26 - B.

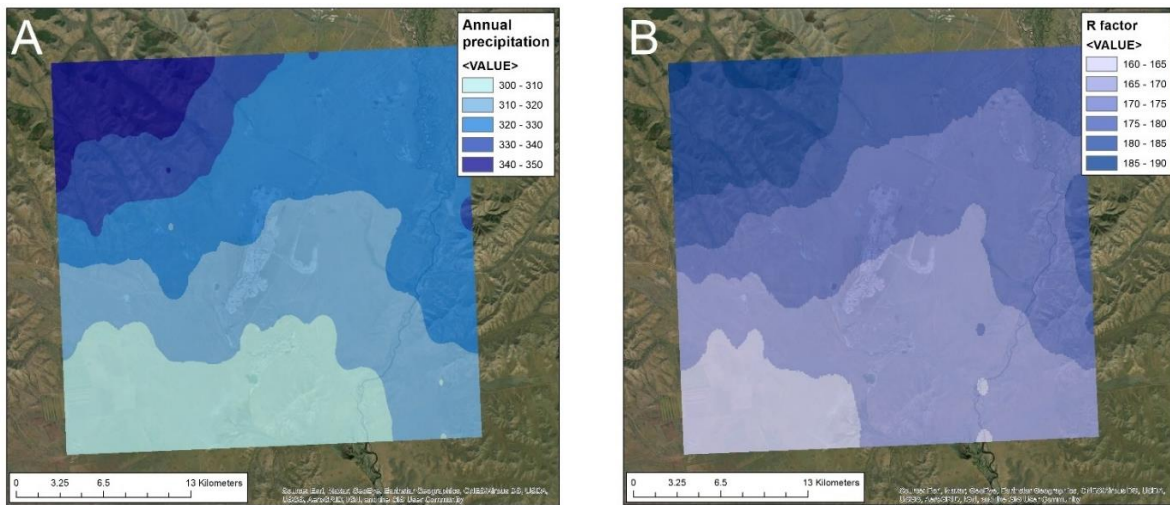


Figure 26. A: Average annual precipitation of Baganuur in [ $\text{mm}\cdot\text{year}^{-1}$ ], B: R factor of Baganuur in [ $\text{MJ}\cdot\text{mm}\cdot\text{h}^{-1}\cdot\text{ha}^{-1}\cdot\text{year}^{-1}$ ]

### 3.2.2 Soil erodibility (K factor)

Soil erodibility factor is directly related to the soils natural resistance to dislodging and displacement due to rainfall and runoff. K factor can be determined by conducting a field survey and assigning K factor values based on soil texture class and organic matter content or it can be determined by calculating using a soil classification map such as the FAO Digital Soil Map of the World. In equation, it is represented as ( $\text{METRIC tons}\cdot\text{ha}\cdot\text{hour}\cdot\text{MJ}^{-1}\cdot\text{ha}^{-1}\cdot\text{mm}^{-1}$ ) [28]. For this paper we will be using two separate K factor values derived from the aforementioned methods and identify the discrepancy between them.

The first K factor value show in Figure 27 was taken from Enkhjargal (2022), which was the result of a field survey conducted around Baganuur area. This survey identified the soil texture class and OM% of around 48 to 50 points and created a raster data set by using interpolation. From this data set, we can interpret that most the soil around the Baganuur area is sandy loam mixed with some loamy sand.

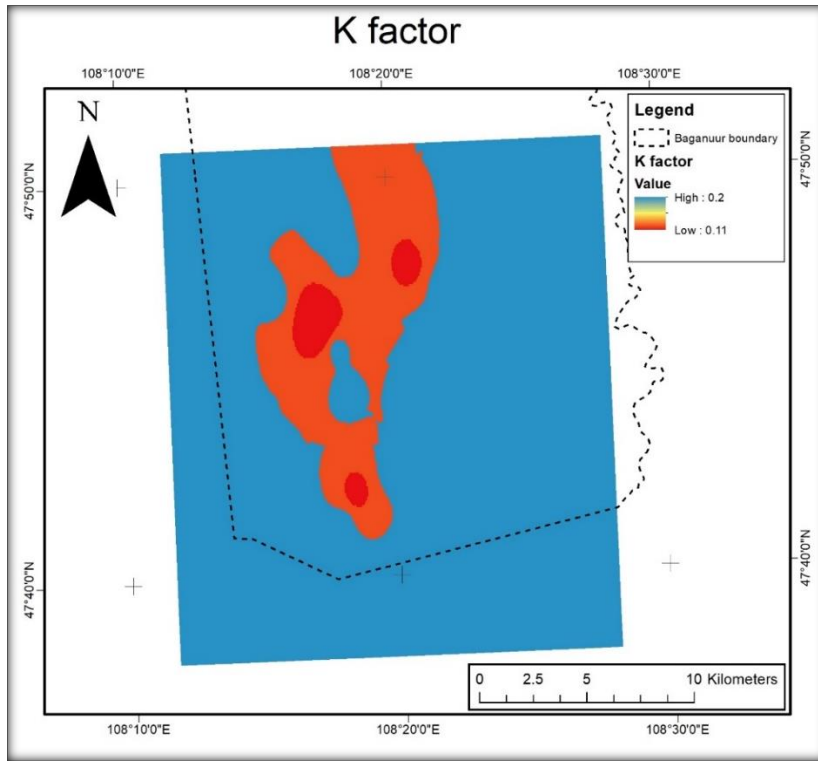


Figure 27. K factor of Baganuur area, determined via field survey and soil texture identification.

The second K factor is determined by obtaining soil classification data from FAO and calculating using equation (3). This advanced formula for K factor suggested by Williams, calculates soil erodibility factor from only 2 properties: soil particle size distribution and organic matter content (Table 3) [29]. For the purpose of differentiation, K factor calculated from equation (3) will be referred to as  $K_{USLE}$ .

$$K_{USLE} = F_{csand} * f_{cl-si} * f_{orgc} * f_{hisand} \quad (3)$$

$$f_{csand} = 0.2 + 0.3 * \exp \left[ -0.256 * m_s * \left( 1 - \frac{m_s}{100} \right) \right] \quad (4)$$

$$f_{cl-si} = \left( \frac{m_{silt}}{m_c + m_{silt}} \right)^{0.3} \quad (5)$$

$$f_{orgc} = 1 - \frac{0.25 * orgC}{orgC + \exp[3.72 - 2.95 * orgC]} \quad (6)$$

$$f_{hisand} = 1 - \frac{\left(0.7 * \left(1 - \frac{m_s}{100}\right)\right)}{\left(1 - \frac{m_s}{100}\right) + \exp\left[-5.51 + 22.9 * \left(1 - \frac{m_s}{100}\right)\right]} \quad (7)$$

Table 3. K<sub>USLE</sub> factor parameters

K factor parameters	Description	Range
m <sub>s</sub>	sand fraction content	0.05-2.00 mm diameter [%]
m <sub>silt</sub>	silt fraction content	0.002-0.05 mm diameter [%]
m <sub>c</sub>	clay fraction content	<0.002 mm diameter [%]
orgC	organics carbon content	[%]

The FAO global soil classification map shows that the soil in our study area is composed of two main soils which are Luvic Castanozems (Kl) and Lithosols (I) where the topsoil properties are given in (Table 4).

Table 4. Topsoil properties of Luvic Castanozems and Lithosols derived from the FAO global soil classification

	sand % topsoil	silt % topsoil	clay % topsoil	OC % topsoil
<b>I</b>	58.9	16.2	24.9	0.97
<b>KL</b>	36.7	40.3	23.1	2

Calculating for K<sub>USLE</sub> results in the raster data shown in Figure 28 where the Lithosol and Luvic Castanozems have a K factor value of 0.14 and 0.133 respectively. Although this is a cost effective and faster way of determining soil erodibility in RUSLE, unlike a K factor determined from field survey, it does not give a detailed range of data. In addition, K<sub>USLE</sub> does not factor in the change in topsoil properties due to mining activity and piling of overburdens.

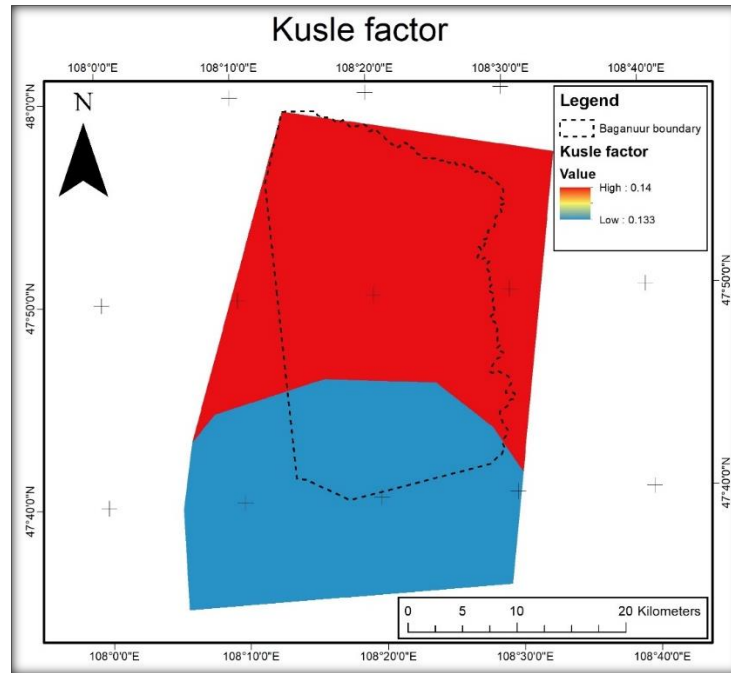


Figure 28. Kusle factor calculated from global soil classification map

### 3.2.3 Topographic steepness factor (LS factor)

Topographic steepness or LS factor is a dimensionless element that represents the effect of slope length (L) and slope steepness (S) on erosion. Slope length in this case depicts the distance between the origin and culmination of an inter rill erosion and is the cause for increasing erosion due to runoff accumulation. On the other hand, slope steepness represents landscape inclination and is tied to erosion rate due to increasing velocity of runoff. [30]

These two elements of LS factor are combined in order to simulate the complex terrain geometry when calculating RUSLE and is represented as equation 8 where first part of the equation reflects slope length and second part of the equation slope steepness.

$$LS = (\chi * \lambda / 22.13)^{0.4} * (\sin\beta / 0.0896)^{1.3} \quad (8)$$

For this paper LS factor is taken from Enkhjargal (2022) due to time constraints. This data is shown in Figure 29.

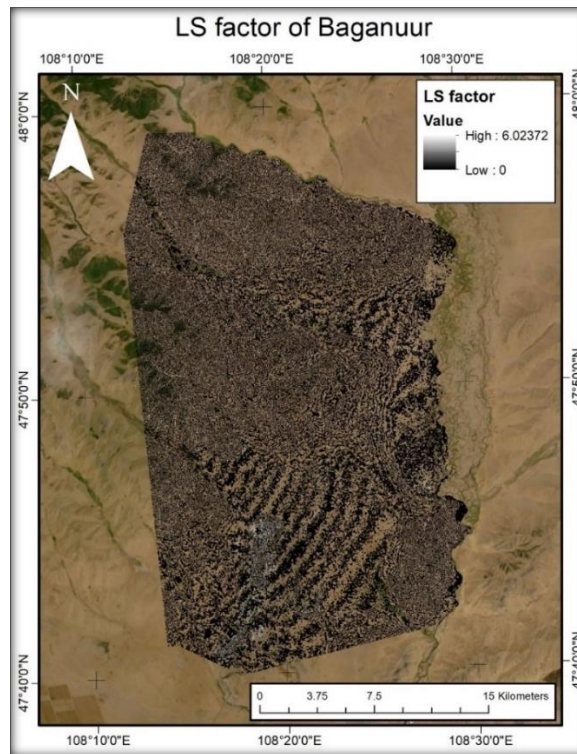


Figure 29. Baganuur LS factor source: Enkhjargal (2022)

### 3.2.4 Land cover and management factor (C factor)

C factor, otherwise known as land cover management factor, is the relationship between vegetation and vulnerability of soil to erosion. C factor is unitless and ranges between 0 to 1 where a value of 1 typically represents bare soil and lower values such a 0.2 representing dense vegetation covers. Water bodies and other similar features will be expressed as 0 [31]. However, it should be noted that since C factor and NDVI is dependent on vegetation, the value will change depending on climatic zone and time of year. For example, because Mongolia has four alternating seasons that affect the growth and presence of vegetation, NDVI and C factor determined in October will be lower than that of July. As seen in Figure 30, most NDVI value for July is between 0.125 and 0.5 while NDVI ranges between 0.5 and 0 in October, indicating a lack of vegetative cover.

While C factor can be determined by conducting a field study and creating a raster file manually, it can also be calculated from Natural Vegetation Difference Index (NDVI) data which is obtainable from United States Geological Survey (USGS) database and Landsat-TM imagery. For this research, we will be suing Landsat-8 imagery which is composed of 11 bands. Each band indicates different ranges of wavelengths in micrometers. NDVI is based on a plant life's ability to reflect near infrared (NIR) and green light [32]. This means NDVI values are reflective of vegetation growth and health. NDVI values range between +1 and -1 where healthy vegetation would result in values near 1. Negative values will

represent bodies of water and values that are close to 0 will represent bare soil or lack of vegetative cover. Thus, NDVI values are calculated as,

$$NDVI = \frac{NIR - IR}{NIR + IR} \quad (9)$$

Where NIR is near infrared indicated as band 5 and IR is red color indicated as band 4 in Landsat-8. In ArcGIS, NDVI can be determined using a pre-given function in the image analysis tools.

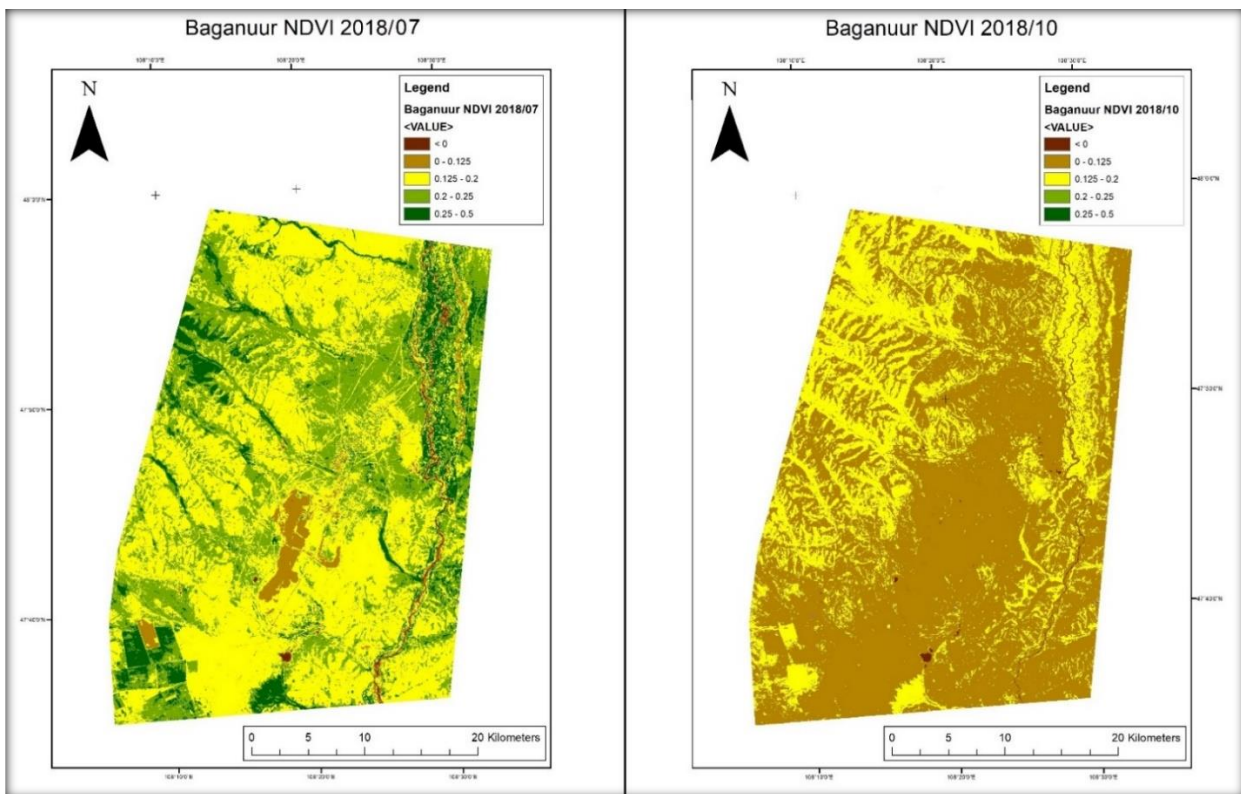


Figure 30. NDVI value of Baganuur in October and July

C factor is calculated from NDVI with the following equation (10) using **Raster Calculator** from **Spatial analyst tools**. This equation suggested by *Durigon et al* [33], allows for the calculation of C factor directly from NDVI values in regions other than Europe.

$$C = (-NDVI + 1)/2 \quad (10)$$

Calculating for C factor in October and July gives the following result in Figure 31 where C factor ranges between 0.25 – 0.6 for July and 0.38 and 0.6 for October. In addition, bare soils such as the mine overburdens range between 0.46 and 0.48 while water bodies such as the Kherlen river has the highest

C values between 0.48 and 0.6. Healthy vegetation during the summer gives C value anywhere between 0.25 and 0.4 while decaying vegetation during fall seems to range between 0.4 and 0.44. Because C factor calculated from NDVI does not directly differentiate the different types of vegetative covers and instead shows the density of foliage, it is possible to somewhat recognize the types of vegetation covers based on color range. For example, C factor for July shows that forested areas typically range between 0.25 and 0.34 while the grasslands range between 0.34 and 0.4.

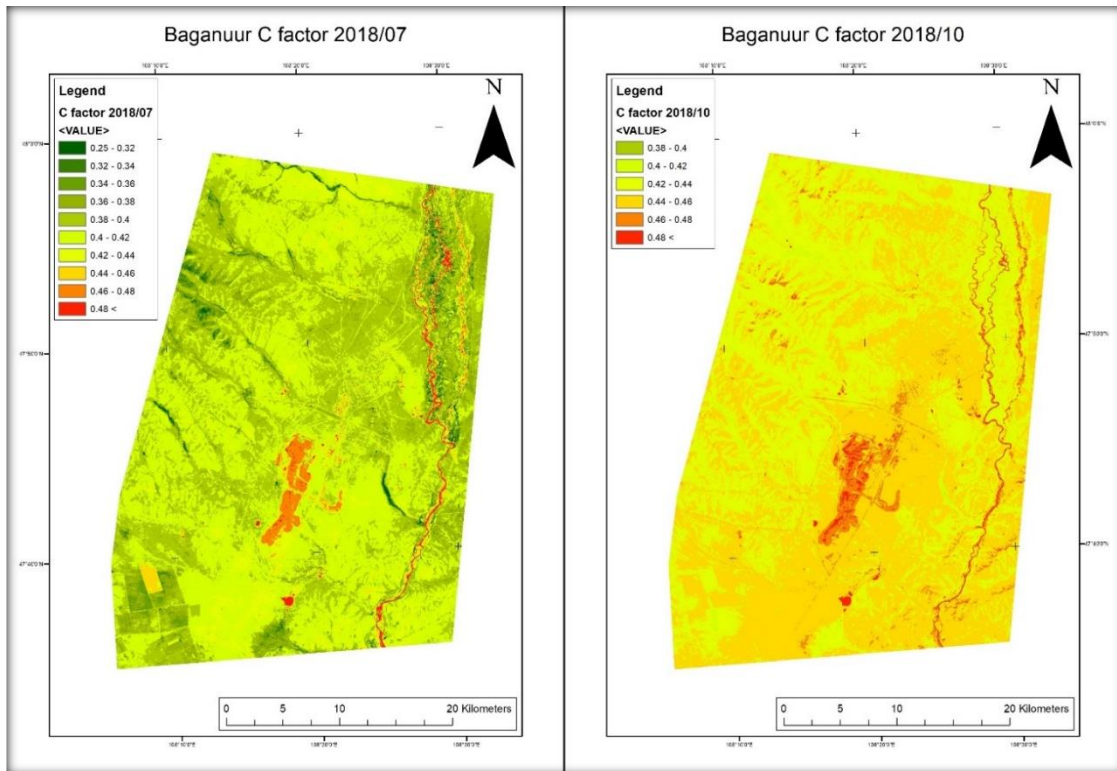


Figure 31. C factor value of Baganuur in October and July

### 3.2.5 Conservation practice (P factor)

Conservation practice factor or P factor represents the influence of soil conservation measures such as re-vegetation and land management techniques such as strip cropping, contouring and terracing on erosion [33]. P factor values change depending on the type of supporting practice and the slope of the landscape where a value of 1 denotes poor or no conservation practice within the area. In addition, slope of landscape has a linear relationship with conservation practice where the increase of slope in percentage increases the value of P factor regardless of conservation practice [34].

Because Baganuur area has little to no supporting practice, all of the study area will have a P factor value of 1.

### 3.3 Morphometry analysis

#### 3.3.1 TPI analysis

TPI is calculated from DEM dataset by using equation 11 in *raster calculator* where irad and orad stands for inner and outer radius respectively and <sf> stands for scale factor, or in this case the neighborhood class. When a certain neighborhood size of TPI is desired the outer radius will be equal to scale factor and inner radius equal to half of that. For example, if a TPI <200> is desired, orad and I rad will be equal to 200 and 100. While it is possible to calculate the entire TPI using equation 11, calculating the focal mean separately using *focal statistics* combining with the original equation gives an easier result. For this research TPI's with a scale factor of 200 and 1000 are calculated (Figure 32). The resulting TPI's can be reclassified into slope classes using threshold shown in Table 5 where SD stands for standard deviation. Slope classes are separated using *map algebra* if ArcGIS and recombined using *mosaic* to create proper detailed map.

$$TPI < sf > = \text{int}((DEM - \text{FocalMean}(DEM, \text{Annulus}, \text{Irad}, \text{Orad})) + 0.5) \quad (11)$$

Table 5. Slope class thresholds for TPI

Class	Slope classes	TPI Threshold
1	Ridge	TPI > +1 SD
2	Upper slope	TPI > 0.5 SD, =< 1 SD
3	Middle slope	TPI > -0.5 SD, < 0.5 SD, slope > 5 deg
4	Flats slope	TPI >= -0.5 SD, =< 0.5 SD, slope <= 5 deg
5	Lower slopes	TPI >= -1 SD, < 0.5 SD
6	Valleys	TPI < -1 SD

In order to create a landform classification map, standard deviation of both TPI 200 and TPI 1000 has to be rounded to approximately 100 using equation 12. The resulting TPI maps can then be used to create landform classes using the TPI thresholds shown in Table 6. This process is done similarly with classifying slope classes with the only difference being multiple condition variables are used to calculate each landforms.

$$TPI < sfi > = int\left(\left(\frac{TPI < sf > - mean}{STDV}\right) * 100\right) + 0.5 \quad (12)$$

Table 6. Landform class threshold for TPI's

Class	Landform	TPI Threshold
1	Canyons, deeply incised streams	(tpi200 <= -100) & (tpi1000 <= -100)
2	Midslope drainages, shallow valleys	(tpi200 <= -100) & (tpi1000 > -100) & (tpi1000 < 100)
3	Upland drainages, headwaters	(tpi200 <= -100) & (tpi1000 >= 100)
4	U-shape valleys	(tpi200 > -100) & (tpi200 < 100) & (TPI1000 <= -100)
5	Plains	(tpi200 > -100) & (tpi200 < 100) & (tpi1000 > -100) & (tpi1000 < 100) & (slope <= 5)
6	Open slopes	(tpi200 > -100) & (tpi200 < 100) & (tpi1000 > -100) & (tpi1000 < 100) & (slope >= 6)
7	Upper slopes, mesas	(tpi200 > -100) & (tpi200 < 100) & ( tpi1000 >= 100)
8	Local ridges, hills and valleys	(tpi200 >= 100) & (tpi1000 <= -100)
9	Midslope drainages, small hills in plains	(tpi200 >=100) & (tpi1000 > -100) & (tpi1000 < 100)
10	Mountain tops, high ridges	(tpi200 >= 100) & (tpi1000 >= 100)

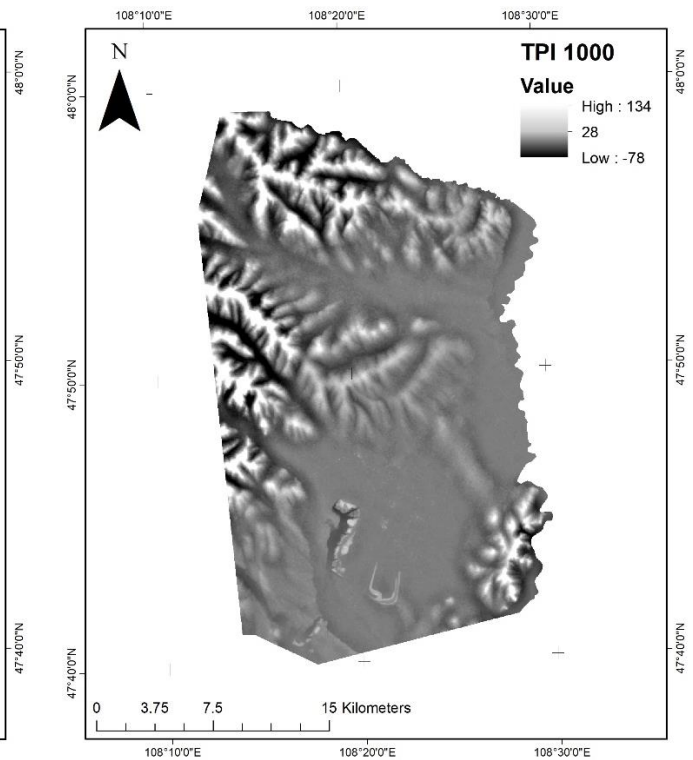
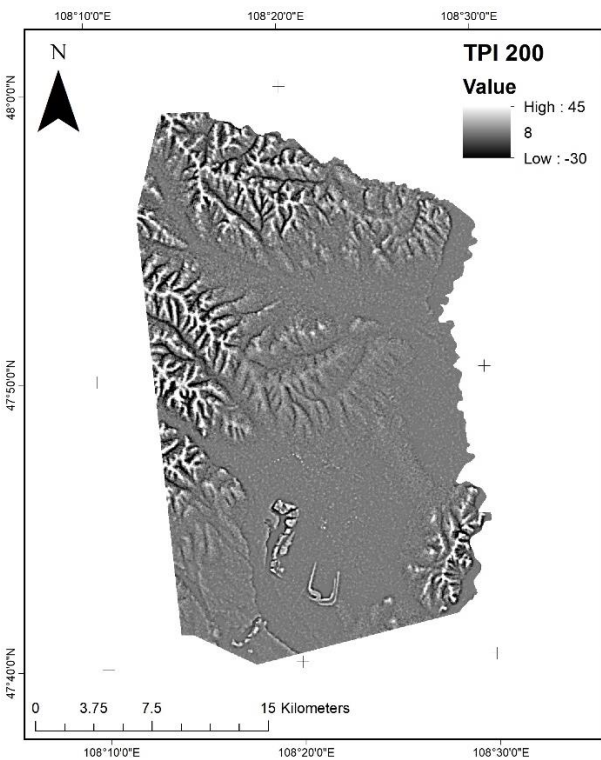


Figure 32. TPI 200 and TPI 1000

### 3.3.2 Watershed analysis

The Baganuur region's watersheds or sub-basins are generated utilizing flow direction and flow accumulation in the ArcGIS application, which has all necessary functionalities. The basic watershed is made up of drainage divisions, stream networks, and outflow points, as discussed previously in the Geomorphology section. The stream networks are depicted by white lines with values ranging from 10'000 to 10'474'900 in ArcGIS, and outlet points are estimated using converging flow accumulation lines (Figure 33). These output points are manually selected and created as point shapefile within the desired converging stream network. It is critical that the outlet point be placed inside the white line rather than outside of it.

Furthermore, because certain watershed outlet points are located outside of the Baganuur boundary, it is preferable to work on a flow accumulation and direction map that not only covers the Baganuur area but also the surrounding area. After an ideal outlet point is located, a sub-basin is created using the **watershed** function of **spatial analyst toolbox** in ArcGIS.

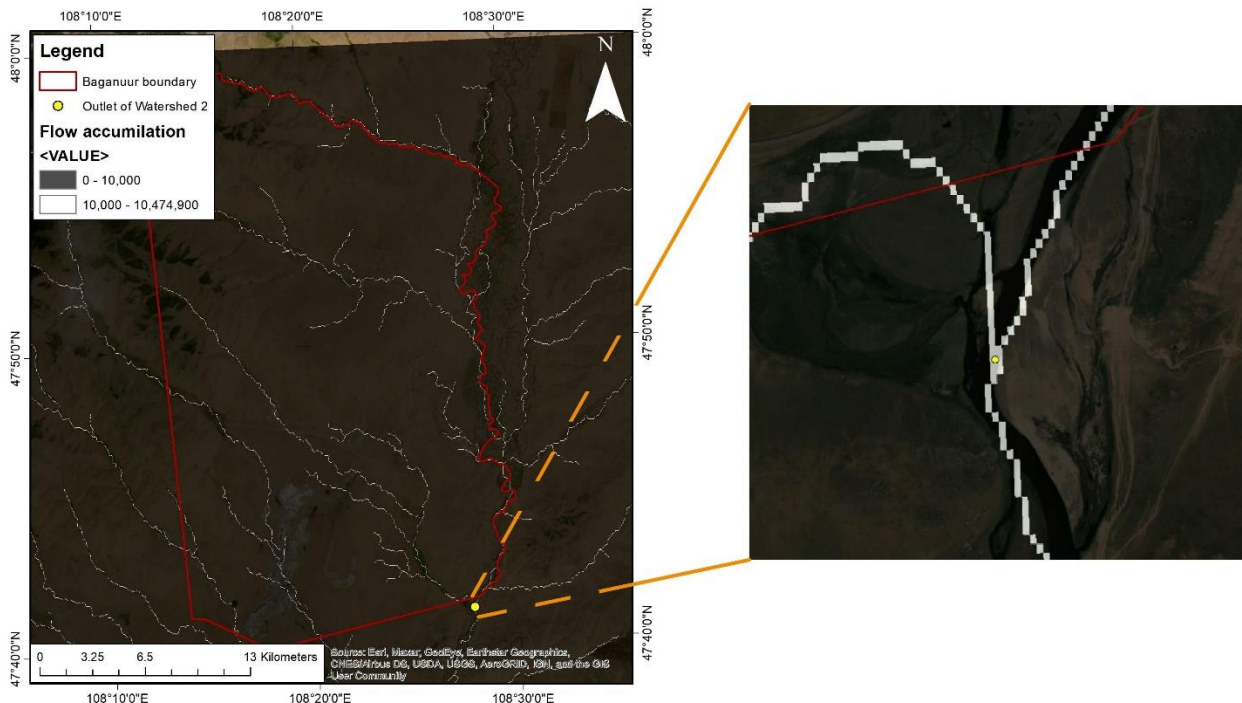


Figure 33. Outflow point example of watershed 2

## 4 Results & Discussion

### 4.1 TPI based slope & landform classification

The resulting landform classification maps show the difference between determining landforms with a single TPI value and generating a more complex landform map with a combination of two TPIs. The Baganuur area is divided into six separate landforms, as shown in Figure 34. It is clear from this that the lower TPI 200 with the smaller neighborhood can better depict minor features like ridges. However, it is not able to distinguish between valleys and lower slopes and misidentifies minor outcrops and open slopes in plains as mountain ridges due to its limited radius. TPI1000, on the other hand, is better at identifying big open landscapes like plains and valleys since its neighborhood radius is significantly larger. Comparing the % coverage of each landforms shown in (table...) we see that the largest increase of landforms in TPI1000 are lower slopes (4.28 %) followed by valleys (2.35 %) and ridges (2.08). In contrast the percent coverage of flat slopes decrease by 5.6%

Additionally, because TPI-based landforms are defined only by their position index, there is no distinction made between natural landscape and mining areas. Regardless of the size of the neighborhood, the waste tips of the coal mine are always identified as mountain ridges, and dug depressions are always identified as valleys, as shown in Figure 34 A and B. As a result, the % coverage of ridges, valleys, lower slopes and upper slopes increase for both maps. A separate examination focused just on the mining region, on the other hand, could be useful in distinguishing between overburdens, trash tips, and excavates sites.

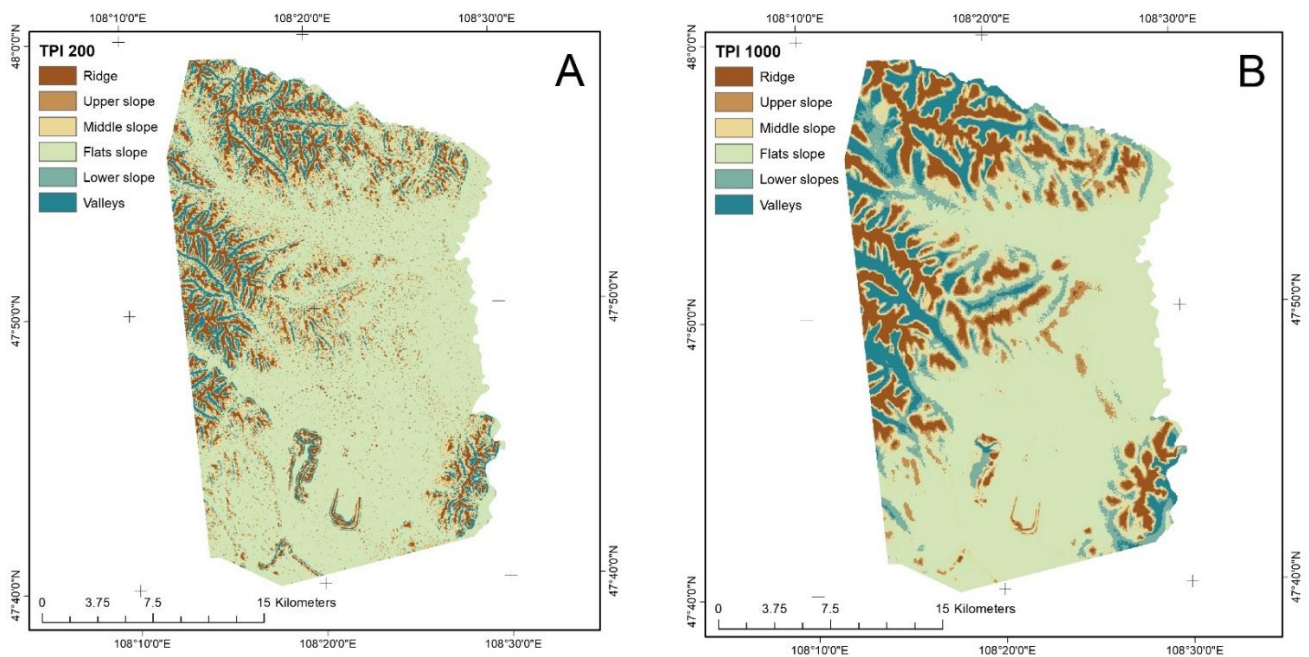


Figure 34. Landform classification derived from TPI200 (A) and TPI1000 (B)

Table 7. Cell count and % coverage of each landform class of landform classification of TPI200 and TPI1000

Class	Landforms	TPI 200		TPI 1000	
		Count	% Coverage	Count	% Coverage
1	Ridge	76500	8.69	94827	10.77
2	Upper slope	62240	7.07	57229	6.50
3	Middle slope	112065	12.72	89671	10.18
4	Flats slope	523394	59.43	474134	53.83
5	Lower slopes	47840	5.43	85532	9.71
6	Valleys	58695	6.66	79341	9.01

Figure 35 shows the result of landform classification that is extrapolated from two separate TPI's and 10 landform classes. Compared to the previous maps which were based on 6 distinct landforms, the combined TPI landform classification allows for 10 landform classes and provides a better detail. This mapping indicates that a majority of the Baganuur area (~67%) consists of plains and open slopes (~11.36%). The rest of the landscape (~21.64%) is made up of various mountain features such as mountain tops/ridges (2.88%), midslope drainages/shallow valleys (3.98%), canyons (2.48%) etc.

## Land type and classification

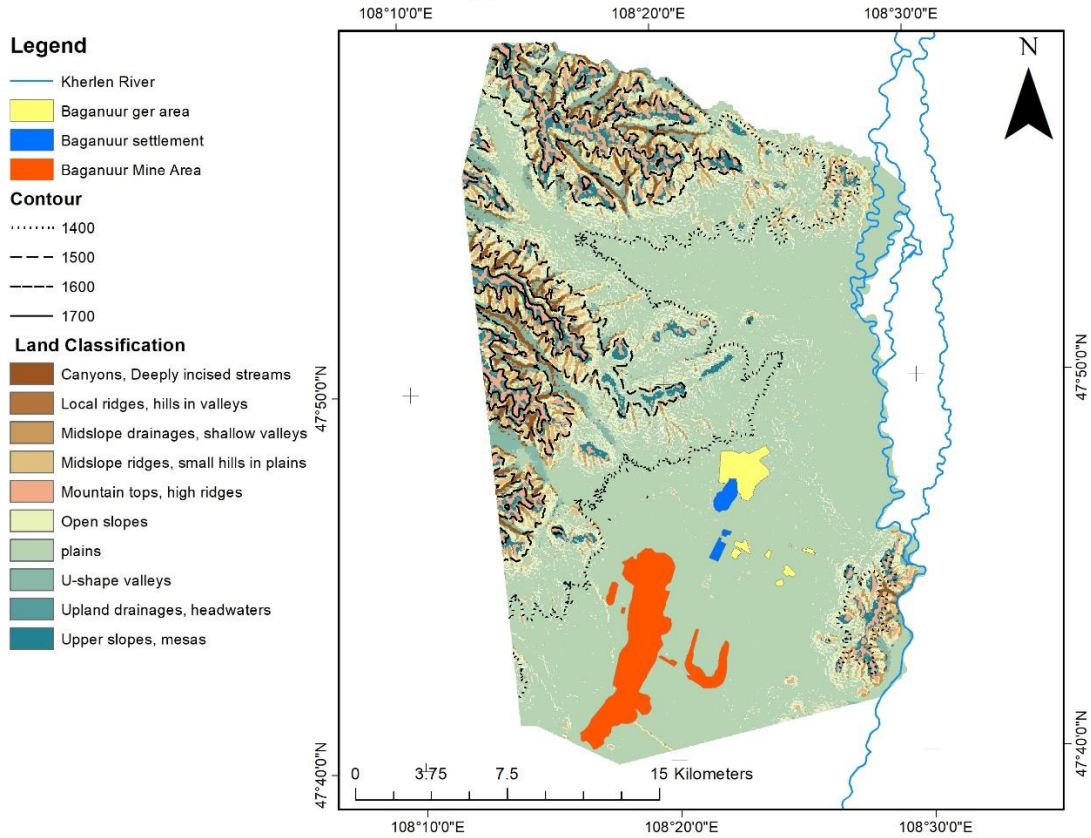


Figure 35. Landform classification based on combination of TPI200 and TPI1000

Table 8. Cell count and % coverage of each landform class of landform classification based on TPI200xTPI1000

Class	Landform	Count	% Coverage
1	Canyons, deeply incised streams	21025	2.48
2	Midslope drainages, shallow valleys	33733	3.98
3	Upland drainages, headwaters	3937	0.47
4	U-shape valleys	32603	3.85
5	Plains	567140	67.00
6	Open slopes	96145	11.36
7	Upper slopes, mesas	30820	3.64
8	Local ridges, hills and valleys	429	0.05
9	Midslope drainages, small hills in plains	24419	2.88
10	Mountain tops, high ridges	36289	4.29

Figure 36. DEM- derived topographic attributes of Baganuur (A-D)

## 4.2 DEM based watershed analysis

Watersheds of the Baganuur area is determined from Flow direction and flow accumulation, which are calculated from DEM data obtained from the USGS. Flow direction values represent the direction of flow on ground surface while the flow accumulation represents the weight of flow based on flow direction. In other word flow accumulation can represent major or minor stream networks if given a certain threshold. The images A and B shows that the Baganuur region contains several major stream networks that are fed from 4 distinct valleys.

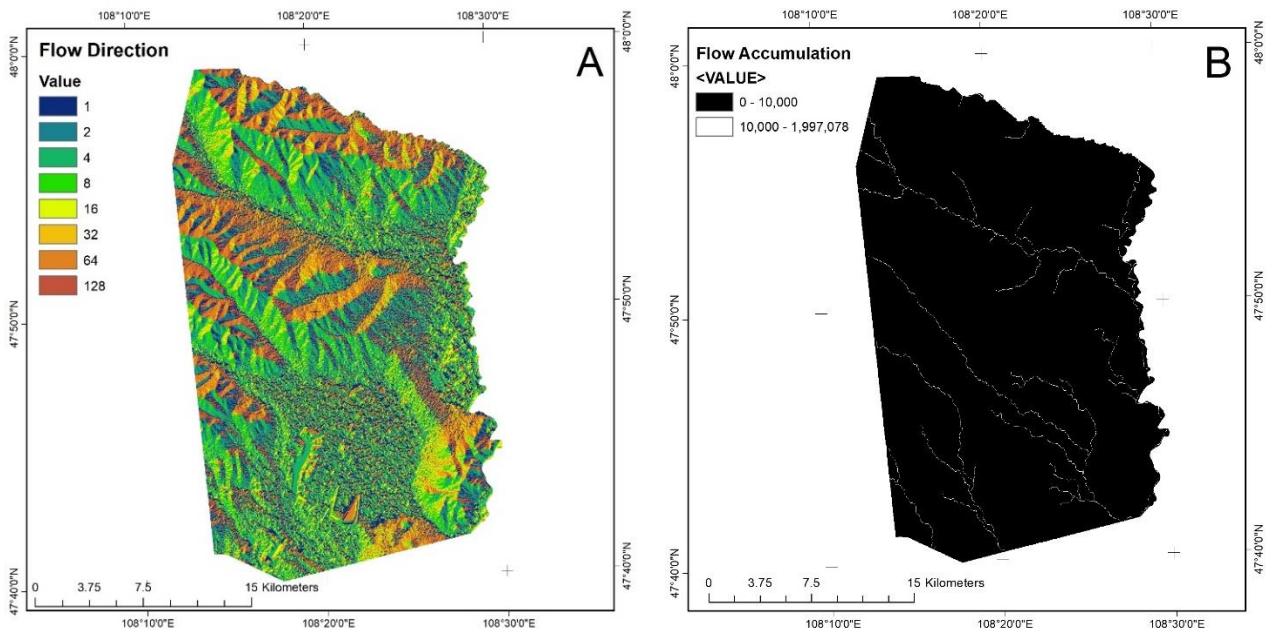


Figure 37. Baganuur flow direction - A, Baganuur flow accumulation - B

The Baganuur area is divided into five separate watersheds based on flow direction and flow accumulation generated by ArcMap's (Figure 38). Watersheds 2 and 3 are contained within the Baganuur district, whilst watersheds 1, 4, and 5 stretch beyond the Baganuur district. These three watersheds run north and north-west of Baganuur, encompassing most of the mountain peaks and valleys. The mountain ranges on the north-west side of Baganuur separate watersheds 1, 2, 4, and 5, while the smaller watershed 3 or subbasin is formed by the prolonged open slope that runs north of the Baganuur settlement and ger areas. In addition, the presence of the Baganuur coal seems alter the flow direction of watershed 1.

The direction of flow is depicted more clearly in (Figure 38), where the direction arrows are constructed using resampled data from (Figure 37 - A). This provides a clearer knowledge of how each ridge is responsible for watershed separation and, more crucially, how the mine affects flow direction. Where

the flow direction would have been consistently directed towards the south-east, it now appears to be split by the mining waste points flowing separately towards the south and east. As a result, watershed 1 might potentially carry additional sediments from the mine's overburdens and waste dumps, thus contaminating the Kherlen river.

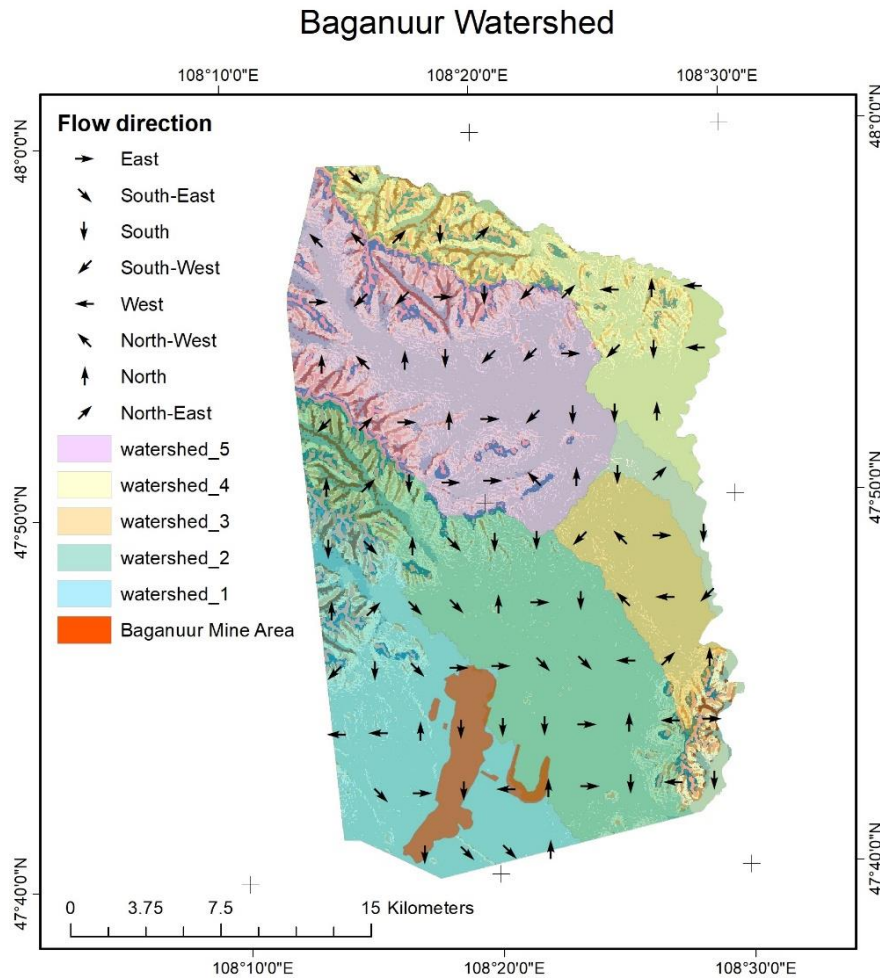


Figure 38. Baganuur watershed mapping

### 4.3 Erosion

All of the pre-determined parameters are used to compute annual soil loss, or (A). A total of four alternative soil loss mappings are constructed to highlight how soil loss fluctuates depending on the stage of vegetation development, K factor derived from fieldwork, and KUSLE computed from remote sensing. However, because the *raster calculator* function excludes any null values and only calculates for data that is available, the resulting soil loss maps only cover the southern parts of Baganuur district (Figure 39).

In this figure very low erosion risks (< 5) are made transparent in order to identify which landforms contain higher soil erosions. Soil loss areas with low (5 - 10) and low medium risk class (10 - 15) are spread throughout open slopes, U-shape valleys and at the base of midslope ridges. Soil losses with medium (15 - 20), high medium (20 - 25) and high-risk classes are located on mountain areas such as canyons, local ridges and midslope drainages.

### Soil loss of 2018/10 with Kusle

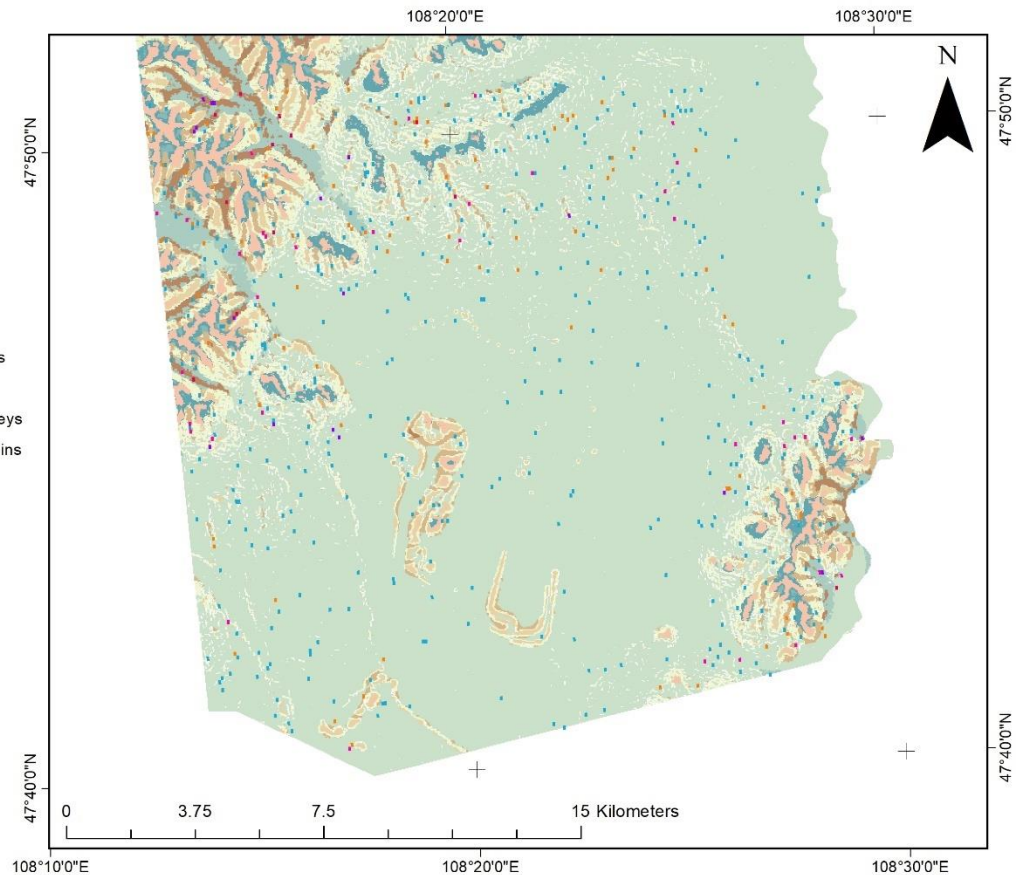


Figure 39. Soil loss of 2018/10 overlaid with landform mapping

- **Soil loss difference for different seasons**

Table 9 shows that the majority of the Baganuur region is at low risk of erosion, with annual soil loss below 10 for both October and July in over 98 percent of the area assessed using K factor and 99 percent of the area calculated using  $K_{USLE}$ . While annual soil loss in October is larger than in July, there is no substantial variation in soil loss ratio between the two. If we look at soil loss calculated using the usual K factor, we can see that October has somewhat higher soil loss values (0.66 percent) than the low and high erosion risk classes. The same pattern can be seen for soil loss calculated from  $K_{USLE}$ .

Table 9. Erosion risk class ratio and their corresponding areas in % for 2018

Soil loss Tons*ha <sup>-1</sup> *year <sup>-1</sup>	Erosion risk class	Soil loss from K [%]		Soil loss from Kusle [%]	
		2018/10	2018/07	2018/10	2018/07
< 5	Very low	95.50	96.17	97.25	97.69
5 - 10	Low	3.22	2.82	1.97	1.69
10 - 15	Low medium	0.79	0.62	0.45	0.38
15 - 20	Medium	0.23	0.19	0.18	0.13
20 - 25	High medium	0.12	0.09	0.08	0.07
25 <	High	0.14	0.12	0.06	0.04

- **Soil loss difference for different K factors**

The greatest significant variation in soil loss estimates is due to changes in K values. Whereas the ratio of erosion risk class is similar for all discoveries, the highest value of each result varies substantially. For July and October, the biggest soil loss computed from normal K is 57.03 and 63.67, respectively, while the maximum values obtained from K<sub>USLE</sub> are 36.18 and 39.4. We can see that these high erosion points are all located in the same places from Annex 2. The soil loss values in the medium erosion risk class (10 - 25 tons\*ha<sup>-1</sup>\*year<sup>-1</sup>) are mostly found on minor hills, depressions, and riverbanks, whereas the high erosion risk locations (> 25 tons\*ha<sup>-1</sup>\*year<sup>-1</sup>) are mostly found between mountain passes. While the greatest soil loss values for each result vary depending on the K factor, soil loss values in the very low risk class (less than 5 tons\*ha<sup>-1</sup>\*year<sup>-1</sup>) do not appear to be significantly affected.

- **Additional findings**

When annual soil loss (A) is calculated using ArcMap's, it seems that certain terrains are left out and displayed as no-data. Figure 40 is the exact same data as Annex 1 but with all of its symbols made translucent. When this is done, specific areas such as settlements, dirt roads, mountain ridges and edges of coal mine waste tips have dark blue checkers over them that display as no data. This was not observable when viewing the image normally and could only be viewed after display quality image has been set to normal or coarse and overlaid with the base map with translucent symbology.

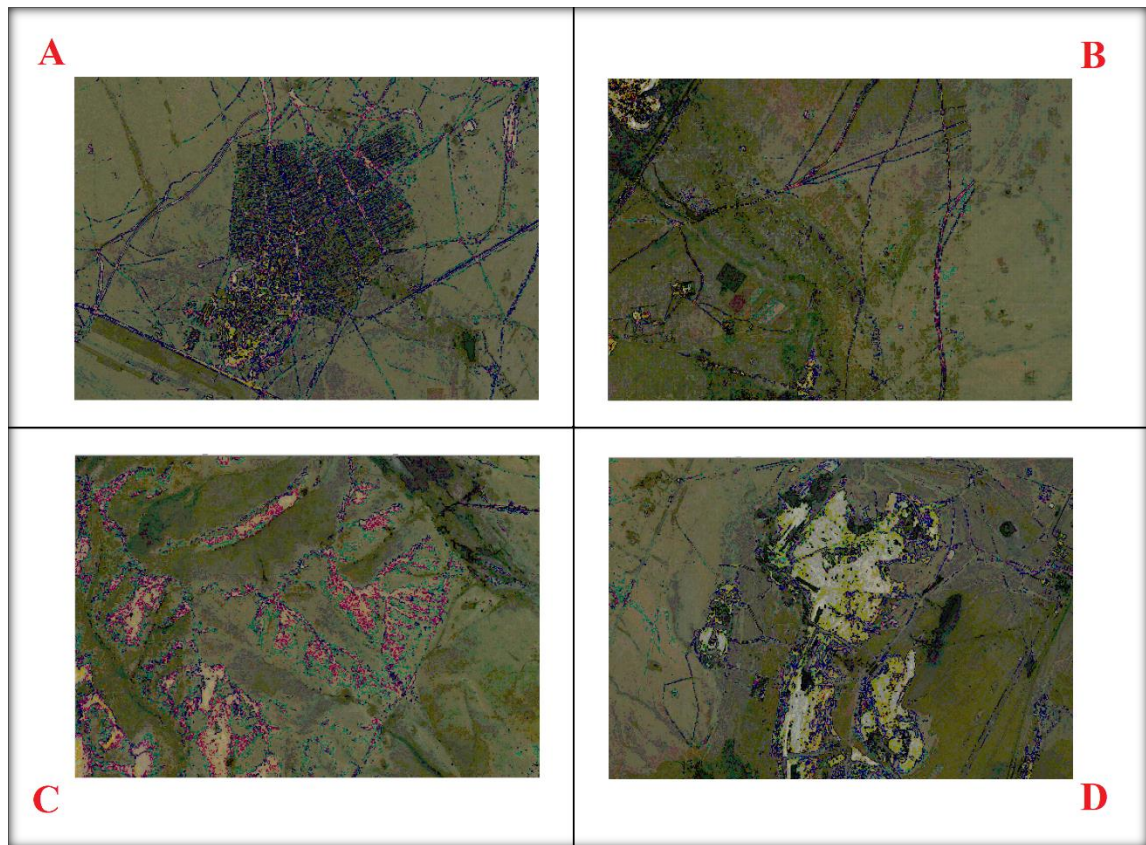


Figure 40. Annex 1 zoomed to a scale of 1:25"000 - A: Baganuur settlement area, B: Dirt roads, C: Mountain ridges, D: North side of the Baganuur open cast mine

## 5 Conclusion

The RUSLE equation was used to quantify soil erosion of July and October of 2018 in the Baganuur area. However, because alternative approaches may be used to generate key RUSLE equation elements, two different soil erodibility factors, K and KUSLE, were utilized in the equation to test the effectiveness of producing a factor solely from satellite imagery data. A morphometric approach was used to complete the second objective of constructing a geomorphological map. Within the Baganuur area, ten distinct landform classes and five distinct sub-basins were found.

While all of the soil loss calculated using the RUSLE equation was under a very low risk hazard ( $< 5 \text{ tons*ha}^{-1}\text{*year}^{-1}$ ), there was a small differential in soil loss between October and July where soil loss for October is roughly higher by  $0.07 \text{ tons*ha}^{-1}\text{*year}^{-1}$ , than July. In both October and July, average soil loss measured using the K factor was ( $\text{tons*ha}^{-1}\text{*year}^{-1}$ ) higher than the KUSLE counter. Other than the minor differences in soil loss values there were no substantial change in soil loss variance and distribution amongst the four erosion maps with low erosions ( $5 - 10 \text{ tons*ha}^{-1}\text{*year}^{-1}$ ) distributed evenly throughout the plains and soil loss higher than medium risk class ( $> 15 \text{ tons*ha}^{-1}\text{*year}^{-1}$ ) located on valleys, ridges and hills of mountains.

Furthermore, while the Baganuur mine does have a prevention method to avoid material washing, watershed and flow direction analyses show that some material from loose overburdens and waste tips may be washed into the Kherlen river through sub-basin 1. More investigation into the soil surface and pollutants in this area could assist in determining if the Baganuur mine truly has an impact on the Kherlen river basin.

Finally, while CORONA satellite photos were successfully georeferenced, the images' nature prevents them from being used for more than a visual comparison at this moment. As a result of this research, a foundation material for future research has been established.

## 6 References

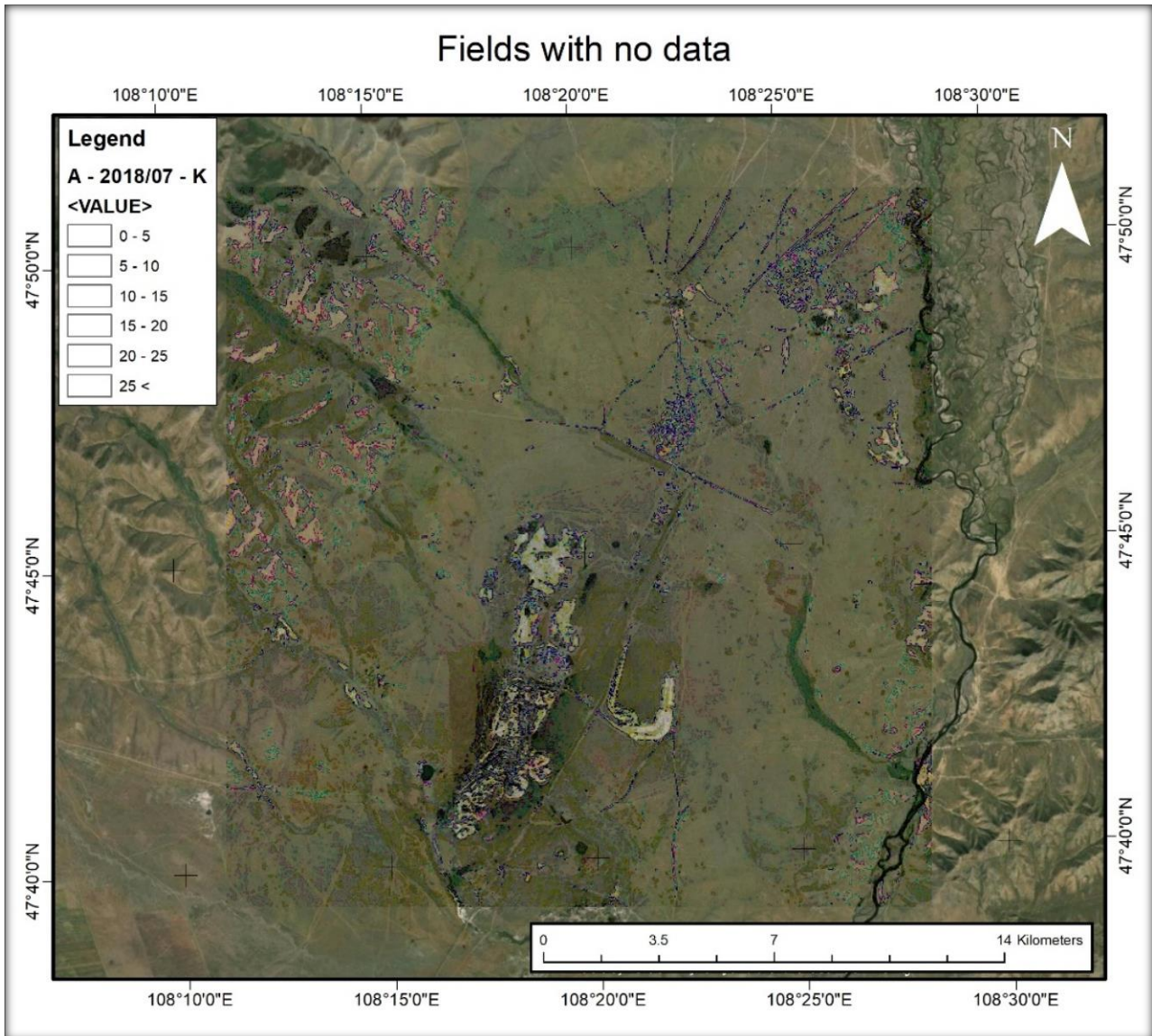
1. Нийслэлийн Статистикийн Газар [Internet]. Нийслэлийн Статистикийн Газар. 2022 [cited 15 May 2022]. Available from: <http://ubstat.mn/>
2. Baganuur mine [Internet]. Global Energy Monitor. 2022 [cited 15 May 2022]. Available from: [https://www.gem.wiki/Baganuur\\_mine](https://www.gem.wiki/Baganuur_mine)
3. Park, J., Kwon, E., Chung, E., Kim, H., Battogtokh, B., & Woo, N. C. (2019). Environmental sustainability of open-pit coal mining practices at Baganuur, Mongolia. *Sustainability*, 12(1).
4. Szypuła, B. (2017). Digital Elevation Models in Geomorphology. *Hydro-Geomorphology - Models and Trends*. <https://doi.org/10.5772/intechopen.68447>
5. Difference between Endogenic and Exogenic Forces in Tabular Format [Internet]. BYJUS. 2022 [cited 15 May 2022]. Available from: <https://byjus.com/free-ias-prep/difference-between-exogenic-and-endogenic-forces/>
6. Stetler, L. D. (2014). Geomorphology. *Reference Module in Earth Systems and Environmental Sciences*.
7. Biswas, A., Das Majumdar, D., & Banerjee, S. (2014). Morphometry governs the dynamics of a drainage basin: Analysis and implications. *Geography Journal*, 2014, 1–14.
8. De Reu, J., Bourgeois, J., Bats, M., Zwertvaegher, A., Gelorini, V., De Smedt, P., Chu, W., Antrop, M., De Maeyer, P., Finke, P., Van Meirvenne, M., Verniers, J., & Crombé, P. (2013). Application of the topographic position index to heterogeneous landscapes. *Geomorphology*, 186, 39–49.
9. Weiss, D. (2001). Topographic Position and Landforms Analysis. The Nature Conservancy
10. Facts About Basins [Internet]. Sciencing. 2022 [cited 15 May 2022]. Available from: <https://sciencing.com/basins-8647463.html>
11. Withanachchi, Sisira & Ploeger, Angelika & Ejarque, Elisabet & Houdret, Annabelle & Nergui, Soninkhishig & Tsogtbayar, Ankhbold. (2014). (Re)configuration of Water Resources Management in Mongolia: A Critical Geopolitical Analysis.
12. How Flow Direction works—ArcGIS Pro | Documentation [Internet]. Pro.arcgis.com. 2022 [cited 15 May 2022]. Available from: <https://pro.arcgis.com/en/pro-app/2.8/tool-reference/spatial-analyst/how-flow-direction-works.htm>
13. How Flow Accumulation works—ArcGIS Pro | Documentation [Internet]. Pro.arcgis.com. 2022 [cited 15 May 2022]. Available from: <https://pro.arcgis.com/en/pro-app/2.8/tool-reference/spatial-analyst/how-flow-accumulation-works.htm>
14. Morgan R. Soil Erosion and Conservation. 3rd ed. Blackwell Science Ltd; 2005.
15. Batkhishig, O. Human Impact and Land Degradation in Mongolia. 2013. Chapter 12. In The volume —Dry land Esat Asia: Land Dynamics Amid Social and Climate Changell. Editors: Jiquan Chen, Shiquang Wan, Geoffrey Henebry, Jiaquo Qi, Garic Gutman, Ge Sun, Martin Kappas. Ecosystem Science and application. The Higher Education Press.
16. Kehew, A. E. (2014). *Geology for engineers and environmental scientists*. Pearson.
17. Montgomery, C. W. (2010). *Environmental geology 9'th edition*. McGraw-Hill Education.
18. Reinhardt, L., Jerolmack, D., Cardinale, B. J., Vanacker, V., & Wright, J. (2010). Dynamic interactions of life and its landscape: Feedbacks at the interface of Geomorphology and Ecology. *Earth Surface Processes and Landforms*, 35(1).
19. Zhao, X., Li, Z., & Zhu, Q. (2017). Change of precipitation characteristics in the water-wind erosion crisscross region on the Loess Plateau, China, from 1958 to 2015. *Scientific Reports*, 7(1).
20. Lóczy, Dénes. (2010). Anthropogenic Geomorphology. 10.1007/978-90-481-3058-0.
21. Keshkamat, S. S., Tsendbazar, N.-E., Zuidgeest, M. H., van der Veen, A., & de Leeuw, J. (2011). The environmental impact of not having paved roads in arid regions: An example from Mongolia. *AMBIO*, 41(2).

22. Kumar, M., Sahu, A. P., Sahoo, N., Dash, S. S., Raul, S. K., & Panigrahi, B. (2022). Global-scale application of the RUSLE model: A comprehensive review. *Hydrological Sciences Journal*, 67(5).
23. Schmidt, M., & Goossens, R. (n.d.). The use of Corona satellite images for generating a high-resolution digital elevation model. *IGARSS 2001. Scanning the Present and Resolving the Future. Proceedings. IEEE 2001 International Geoscience and Remote Sensing Symposium*.
24. Cheng, Y., Tsendeekhuu, T., Narantuya, N., & Nakamura, T. (2008). Phytosociological study of steppe vegetation in Mongolia. *Grassland Science*, 54(3).
25. Dadvadorj, D., Batjargal, Z., Natsagdorj, L. (2014). Mongolia Second Assessment on Climate Change. Ministry of Environment and Green Development of Mongolia
26. World Bank Climate Change Knowledge Portal [Internet]. Climateknowledgeportal.worldbank.org. 2022 [cited 15 May 2022]. Available from: <https://climateknowledgeportal.worldbank.org/country/mongolia/climate-data-historical>
27. Hamandawana, H., Eckardt, F., & Ringrose, S. (2007). Proposed methodology for georeferencing and mosaicking Corona photographs. *International Journal of Remote Sensing*, 28(1).
28. Gelagay, H. S., & Minale, A. S. (2016). Soil loss estimation using GIS and remote sensing techniques: A case of koga watershed, northwestern Ethiopia. *International Soil and Water Conservation Research*, 4(2).
29. Wang, B., Zheng, F., & Guan, Y. (2016). Improved USLE-K factor prediction: A case study on water erosion areas in China. *International Soil and Water Conservation Research*, 4(3).
30. Khassaf, S., & Al Rammahi, A. (2018). Estimation of slope length factor (L) and slope steepness factor (s) of Rusle equation in the Euphrates River watershed by GIS modeling. *Kufa Journal of Engineering*, 9(3).
31. Bouguerra, H., Bouanani, A., Khanchoul, K., & Derdous, O. (2017). Mapping erosion prone areas in the bouhamdane watershed (Algeria) using the revised universal soil loss equation through GIS. *Journal of Water and Land Development*, 32(1).
32. Landsat Normalized Difference Vegetation Index | U.S. Geological Survey [Internet]. Usgs.gov. 2022 [cited 15 May 2022]. Available from: <https://www.usgs.gov/landsat-missions/landsat-normalized-difference-vegetation-index>
33. Durigon, V. L., Carvalho, D. F., Antunes, M. A. H., Oliveira, P. T. S., & Fernandes, M. M. (2014). NDVI time series for monitoring Rusle cover management factor in a tropical watershed. *International Journal of Remote Sensing*, 35(2).
34. Parveen, R., & Kumar, U. (2012). Integrated approach of universal soil loss equation (USLE) and Geographical Information System (GIS) for soil loss risk assessment in Upper South Koel Basin, Jharkhand. *Journal of Geographic Information System*, 04(06).
35. Borrelli P, Robinson D, Fleischer L, Lugato E, Ballabio C, Alewell C et al. An assessment of the global impact of 21st century land use change on soil erosion. *Nature Communications*. 2017;8.
36. Shi H, Gao Q, Qi Y, Liu J, Hu Y. Wind erosion hazard assessment of the Mongolian Plateau using FCM and GIS techniques. *Environmental Earth Sciences*. 2009;61(4):689-697.
37. World Bank Climate Change Knowledge Portal [Internet]. Climateknowledgeportal.worldbank.org. 2022 [cited 15 May 2022]. Available from: <https://climateknowledgeportal.worldbank.org/country/mongolia/climate-data-historical>
38. World Weather Information Service [Internet]. World Weather Information Service. 2022 [cited 15 May 2022]. Available from: <https://worldweather.wmo.int/en/city.html?cityId=1132>
39. Хороо Y. Статистикийн мэдээллийн нэгдсэн сан [Internet]. Үндэсний Статистикийн Хороо. 2022 [cited 15 May 2022]. Available from: <http://1212.mn/>
40. Roy L, Das S. GIS-based landform and LULC classifications in the Sub-Himalayan Kaljani Basin: Special reference to 2016 Flood. *The Egyptian Journal of Remote Sensing and Space Science*. 2021;24(3):755-767.

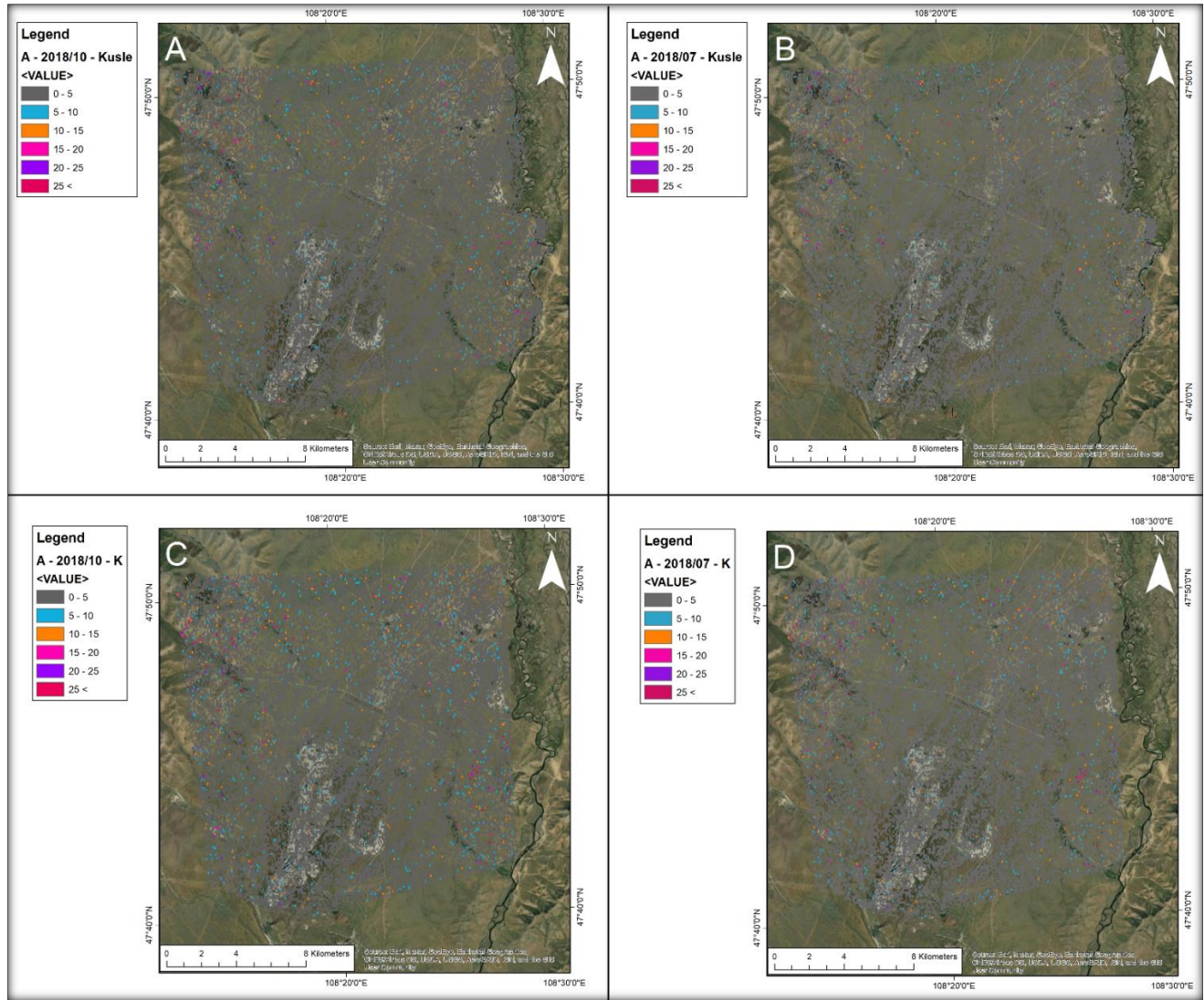
41. Гео-мэдээллийн сан [Internet]. Eic.mn. 2022 [cited 15 May 2022]. Available from: <https://eic.mn/geodata/download.php?count=10&page=3>

42. Okolie, C. (2018). Watershed Analysis and its Applications. 10.13140/RG.2.2.13625.5232

## 7 Appendices



Annex 1. Data on soil loss with display quality set to medium, all values made translucent, and base-map overlain to show empty data fields



Annex 2. RUSLE calculation results A: Soil loss calculated for October 2018 using K<sub>usle</sub>, B: Soil loss calculated for July 2018 using K<sub>usle</sub>, C: Soil loss calculated for October 2018 using K, D: Soil loss calculated for July 2018 using K